12-14-2017

Modeling Rhythm Generation in Swim Central Pattern Generator of Melibe Leonina

Deniz Alacam

Recommended Citation
Alacam, Deniz, "Modeling Rhythm Generation in Swim Central Pattern Generator of Melibe Leonina." Dissertation, Georgia State University, 2017.
https://scholarworks.gsu.edu/math_diss/48

MODELING RHYTHM GENERATION IN SWIM CENTRAL PATTERN GENERATOR OF
MELIBE LEONINA

by

DENIZ ALAÇAM

Under the Direction of Andrey Shilnikov, PhD

ABSTRACT

Central pattern generators (CPGs) are neural networks to produce a rich multiplicity of rhythmic activity types like walking, breathing and swim locomotion. Basis principles of the underlying mechanisms of rhythm generation in CPGs remain yet insufficiently understood. Interactive pairing experimental and modeling studies have proven to be vital to unlocking insights into operational and dynamical principles of CPGs and support the consensus that the most of essential structural and functional elements in vertebrate and invertebrate nervous systems are shared.

We have developed a family of highly-detailed, biologically plausible CPG models using the extensive data intracellularly recorded from constituent interneurons of the swim CPG of the sea slug *Melibe leonina*. We also have deduced fundamental properties needed for the devised Hodgkin-Huxley type neuronal models with specific slow-fast dynamics to become qualitatively and quantitatively similar to biological CPG interneurons and their responses to parameter and external perturbations. We have studied the onset and robustness of rhythmogenesis of network bursting the CPG circuits comprised of tonic spiking interneurons coupled with mixed inhibitory/excitatory, slow chemical synapses. We have shown that the mathematical CPG model can be reduced functionally from an 8-cell circuit to a 4-cell one using the calibration of timing and weights of synaptic coupling between CPG core interneurons.

We demonstrate that the developed mathematical network meets all the experimental fact-checks obtained for the biological Melibe swim CPG from a variety of state-of-the-art experimental studies including dynamic-clamp recordings, external pulses perturbations as well as from its forced behaviors under applications of neuro-blockers such as curare and TTX.

Our model and developed mathematical approaches and computational methodology allow for laying down theoretical foundations necessary for devising new detailed and phenomenological models of neural circuits and for making testable predictions of dynamics of rhythmic neural networks from diverse species.

INDEX WORDS: network dynamics, rhythm generation, Melibe Leonina, sea slug swim CPG, mathematical modeling,swim locomotion, half-center oscillator, sea slug, rhythmogenesis, bifurcation analysis, slow synapses, modular networking

MODELING RHYTHM GENERATION IN SWIM CENTRAL PATTERN GENERATOR OF MELIBE LEONINA

by

DENIZ ALAÇAM

A Dissertation Submitted in Partial Fulfillment of the Requirements for the Degree of

Doctor of Philosophy

in the College of Arts and Sciences

Georgia State University

2017

MODELING RHYTHM GENERATION IN SWIM CENTRAL PATTERN GENERATOR OF MELIBE LEONINA

by

DENIZ ALAÇAM

Committee Chair:	Andrey Shilnikov
Committee:	Igor Belykh
	Vladimir Bondarenko
	Paul Katz

Electronic Version Approved:

Office of Graduate Studies

College of Arts and Sciences

Georgia State University

December 2017

DEDICATION

This dissertation is dedicated to my family and friends, without whom none of my success would be possible.

ACKNOWLEDGMENTS

I would like to express my most profound gratitude to my advisor and committee chair Dr. Andrey Shilnikov for believing in me, supporting and guiding me during all these years. He will always be a great role model for me. I would like to acknowledge and thank the rest of my dissertation committee members: Dr. Igor Belykh, Dr. Vladimir Bondarenko, and Dr. Paul Katz for their time, guidance, and recommendations.

Special thanks to Dr. Akira Sakurai for providing the experimental data for this study, and being always kind and helpful during my studies.

Finally, I would like to acknowledge the great people that I worked with in Shilnikov Lab: Aaron Kelley, Krishna Pusuluri, Huiwen Ju, Jassem Bourahman, Jack Scully, Dr. Jarod Collens, Dr. Tingli Xing, Dr. Jeremy Wojcik, Dr. Justus Schwabedal and Drake Knapper. They have always been inspiring, supporting, helpful and true friends to me. I would like to thank especially Krishna and Huiwen for all their contribution, and hard work for this project.

Thank you all.

TABLE OF CONTENTS

LIST OF TABLES

LIST OF FIGURES

LIST OF ABBREVIATIONS

CPG - Central Pattern Generators

FTM - Fast Threshold Modulations

SNIC - Saddle Node on Invariant Circle

AH - Andronov-Hopf

PIR - Post Inhibitory Rebound

Si1 - Swim interneuron 1

Si2 - Swim interneuron 2

Si3 - Swim interneuron 3

Si4 - Swim interneuron 4

CHAPTER 1

INTRODUCTION

Mathematical models are commonly used tools in a wide variety of disciplines both in natural sciences (physics, chemistry, biology) and applied sciences (engineering, economics, sociology, computer science, etc.). These powerful tools are highly efficient for studying, analyzing, understanding and predicting the behavior of complex structures. The complexity of biological structures have been an attractive area for mathematical modeling, and biologically plausible models have provided significant benefits in various fields such as robotics, developing drugs and treatments, understanding population and network dynamics.

Emergent behavior of biological models is an increasingly popular topic in the field of biology, mathematics, and engineering. One of the areas where mathematical models are substantially used is neuroscience. A plethora of vital rhythmic motor behaviors, such as heartbeat, respiratory functions, and locomotion are produced and governed by neural networks called central pattern generators (CPGs) [1, 2, 3, 4, 5]. A CPG is a microcircuit of interneurons whose mutually synergetic interactions autonomously generate an array of multi-phase bursting rhythms underlying motor behaviors. There is a growing consensus in the community of neurophysiologists and computational researchers that some basic structural and functional elements must be shared by CPGs in invertebrate and vertebrate animals. As such, we should first understand these elements, find the universal principles, and develop efficient mathematical and computational tools for plausible and phenomenological models of CPG networks. Pairing experimental studies and modeling studies have proven to be key to unlocking insights into operational and dynamical principles of CPGs [6, 7, 8, 9, 10, 11, 12, 13]. Although various circuits and models of specific CPGs have been developed, it remains unclear what makes the CPG dynamics so robust and flexible [14, 15, 16, 17, 18, 19]. It is also unclear what mechanisms a multi-functional motor system can use to generate polyrhythmic outcomes to govern several behaviors [20, 21, 22]. The goal of this study is to gain insight into the fundamental and universal rules governing pattern formation in complex networks of neurons. To achieve this goal, we should identify the rules underlying the emergence of cooperative rhythms in simple CPG networks.

Recently, many computational studies have been focused on a range of 3-cell motifs of bursting neurons coupled by chemical (inhibitory and excitatory) and electrical synapses to disclose the role of coupling in generating sets of coexisting rhythmic outcomes, see [23, 24, 22, 25, 26] and references therein. These network structures reflect the known physiological details of various CPG networks in real animals. Next, we would like to explore dynamics and stability of some identified CPG circuits constituted by 4-cells [27]. Examples of such sub-networks can be found in the crustacean stomatogastric ganglion (STG) [1, 28, 29, 19], as well as in the swim CPGs of the sea slugs – *Melibe leonina* [30] (depicted during swimming in Fig. 1.1) and *Dendronotus iris* [31, 32, 33, 34]. Our greater goal is to create dynamical foundations for the onset, morphogenesis and structural robustness of rhythmic activity patterns produced by swim CPGs in these animals. The modeling process of developing a highly detailed mathematical model of the *Melibe* swim CPG will be discussed in this study.

In this chapter, introductory information about the network configuration of the Melibe swim CPG, identification process, and previous and ongoing neurophysiological studies about the CPG as well as the previous mathematical modeling studies will be presented.The details of the network features will be provided in later chapters.

Figure 1.1: Melibe Leonina swims with rhytmic behavior of flexing its body laterally left and right. Figure provided courtesy of Melisa Beveridge

In the second chapter, the early stages of mathematical modeling of Melibe swim CPG is presented. We used a reduced form of the biological swim CPG in mathematical modeling. The reduction process of biological CPG is introduced in this chapter. In the light of experimental recordings of the time, we considered that all cells in CPG as identical cells. They are all modeled as tonic spiking cells with same intrinsic dynamics. The synapses are modeled with fast threshold modulation (FTM) avoiding most details of characteristic features for each synapse. Different synapse types are implemented into the model by variation of coupling strengths (strong or weak) and reversal potentials (inhibitory or excitatory) . Our goal for this chapter is to generate what we called 3/4-phase shift in control case. As we received more experimental data, we understood more of the working mechanism of the network and realized that the network has much more features than 3/4-phase shift.

In the third chapter, through the experimental studies, we have realized that the cells have different intrinsic dynamics and two HCOs forming the CPG follow different mechanisms to generate anti-phase bursting. Also the previous model, failed to capture all features of the network. According to the experimental findings, we have modeled one pair of interneurons as tonic spikers and the other pair as hyperpolarized quiescent cells. In order to make the model biologically more plausible, the synapses are modeled as alpha synapses. FTMs are fast synapses as indicated in the name and they represent either a fully on or off synapses. Unlike FTMs, alpha synapses exhibit more realistic dynamics. After the changes in the model, we saw that the model captures more features of the network but according to the current experimental results, we had to modify the mathematical model again.

The fourth chapter covers the final version of the mathematical model for Melibe swim CPG. The latest experimental results showed that all cells used in the mathematical network are tonic spikers but still they have different intrinsic dynamics such as spiking frequency. Intrinsic dynamics of all cells are set according to the experimental results. Besides alpha synapses, we used a dynamic synapse for modeling the slow contralateral excitatory synapse.

The final chapter summarizes the significance of study, presents the conclusions. Also relevance and significance of the future directions are discussed.

1.1 Melibe Swim CPG

The nudibranch mollusk *Melibe Leonina* swims by flexing its body laterally to left and right. Studies on identifying the CPG which is believed to be in control of swim locomotion of the sea slug have been going on over a decade [35]. The Melibe swim CPG is one of the few CPGs which can be described in detail and with a known function. Earlier studies on idenfiying Melibe swim CPG proposed that it is a very simple circuit of two pairs of swim interneurons (Sis) [35]. The interneurons are labeled as swim interneurons 1 (Si1) and swim interneuorons 2 (Si2) and their locations in the brain is shown in Fig. 1.2 (a). One of each pair is located on contralateral parts of the brain and each pair of interneurons form a half-center oscillator(HCO) where neurons are connected thorough reciprocal inhibitory connections [36]. A diagram representation of initial CPG motif is shown in Fig. 1.2(b). HCOs are a commonly seen small cell configuration in CPGs and the cells can generate rhythmic activity in anti-phase through HCO configuration while they provide no rhythmic output when they are in isolation. In the Melibe swim CPG, it is observed that the contralateral interneurons burst in anti-phase and this rhythm was related to the swim pattern of the animal in early studies.

In later studies, in addition to previously identified two pairs of swim interneurons (Si1s and Si2s), two more pairs of interneurons were discovered in the CPG. They are named similar to the previously identified cells, swim interneuron 3 (Si3) and swim interneuron 4(Si4). The discovery of new pairs of interneurons revealed that the configuration of circuit is beyond a classical HCO set up. Thompson and Watson [35] proposed that the initially

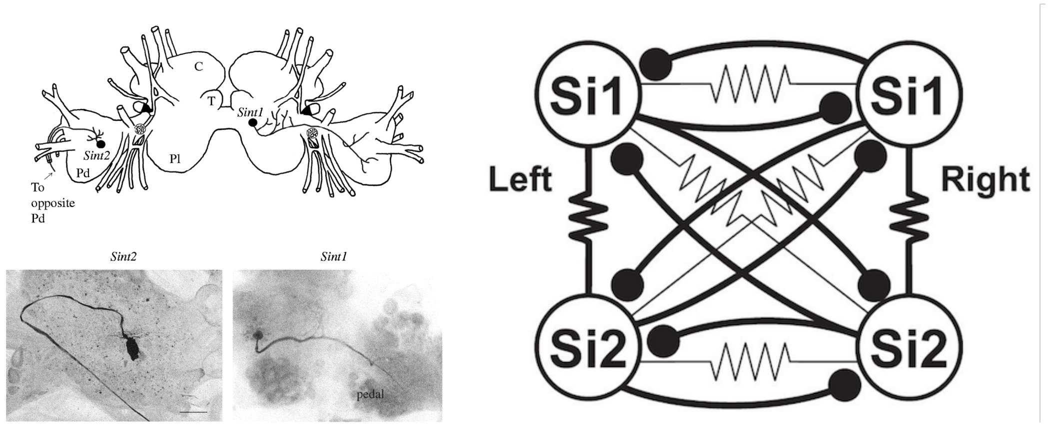

(a) (b)

Figure 1.2: (a) Locations of Si1s and Si2s in Melibe brain according to the early results of identification studies [35] (b) CPG motif of Melibe swim CPG for early results. Courtesy A.Sakurai

discovered circuit is the core of the CPG and there are no other interneurons involved in the CPG. With the new findings, complexity of the circuit was carried to a new level. Detailed connection diagram of the current CPG is given in Fig 1.3. Each contralateral pair is connected through reciprocal inhibitory synapses, in other words form HCOs. In addition to the reciprocal inhibitions, there are also ipsilateral and contralateral one way inhibitory synapses.

In addition to inhibitory synapses in the circuit, there are also excitatory and electrical connections. Full details of the model and synapses are given in [30]. Each connection has its own characteristic and specific features of each connection has crucial importance for mathematical modeling. Using these features, we designed a reduced network for mathematical modeling. The mathematical network contains four cells instead of eight cells in the biological network. The reduction process is explained in detail in chapters 2,3 and 4.

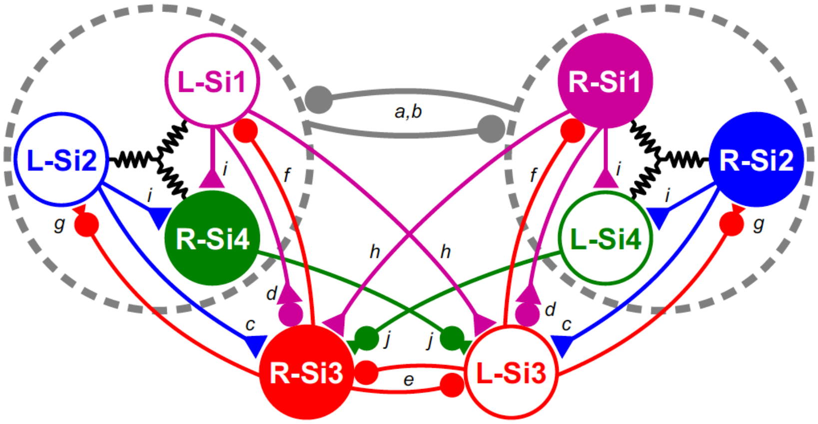

Figure 1.3: Recent CPG diagram of Melibe swim CPG with inhibitory (●), excitatory (◄) and electrical (\/\/) synapses [30]. The filled cells are located on right side of the brain and the unfilled ones are located on the left side of the brain. The previously identified cells(Si1s and Si2s) and Si4s are circled by gray dashed line and the inhibition between contralateral pairs is represented by the gray inhibitory connections between the circles. The wiring diagram provided courtesy of A. Sakurai.[30]

1.2 Previous Modeling Studies

In earlier stages of experimental studies, it was proposed that one of the most significant features of the CPG is the phase locked network bursting during active swimming. As a result, the mathematical modeling studies focused on the generation, stability and robustness of this particular rhythm.

Earlier experimental studies did not provide information about the characteristics of the individual cells in isolation. For modeling studies, each cell is assumed to be an intrinsic burster so the choice of model was leech heart interneuron model which is a Hodgkin-Huxley type model and developed for endogenously bursting heart interneurons. The earlier network diagram is used for modeling studies and synapses were modeled with alpha synapses.

This configuration was sufficient for rhythm generation and showed the stability and

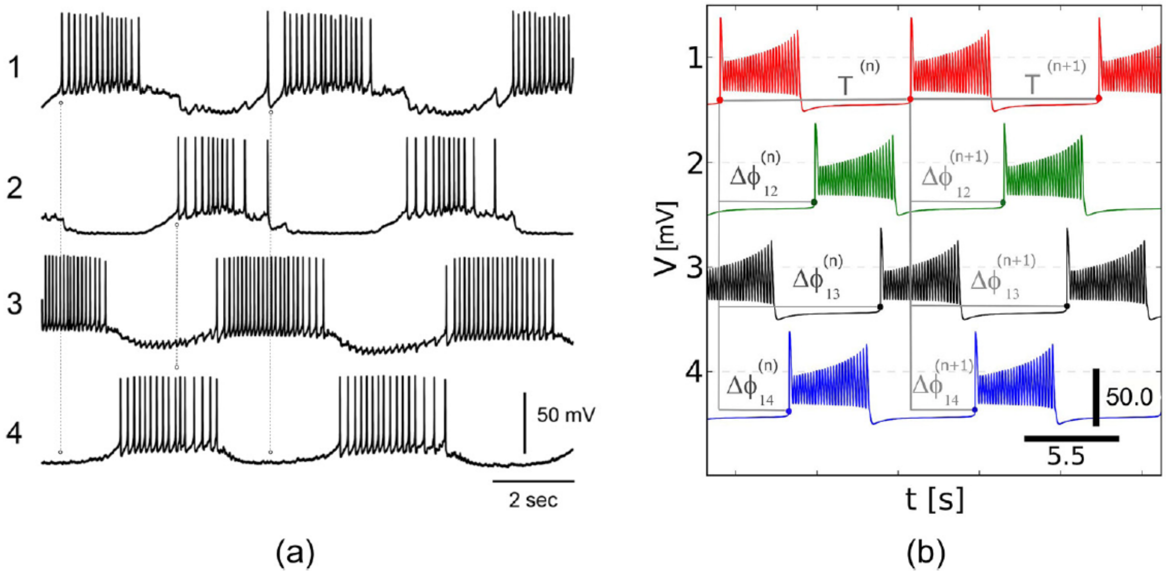

Figure 1.4: (a) Network bursting recorded from Si1s and Si2s during the swimming activity. Recordings provided courtesy of A. Sakurai. (b) The voltage traces generated by the leech interheart model where individual cells are intrinsic bursters.[27]

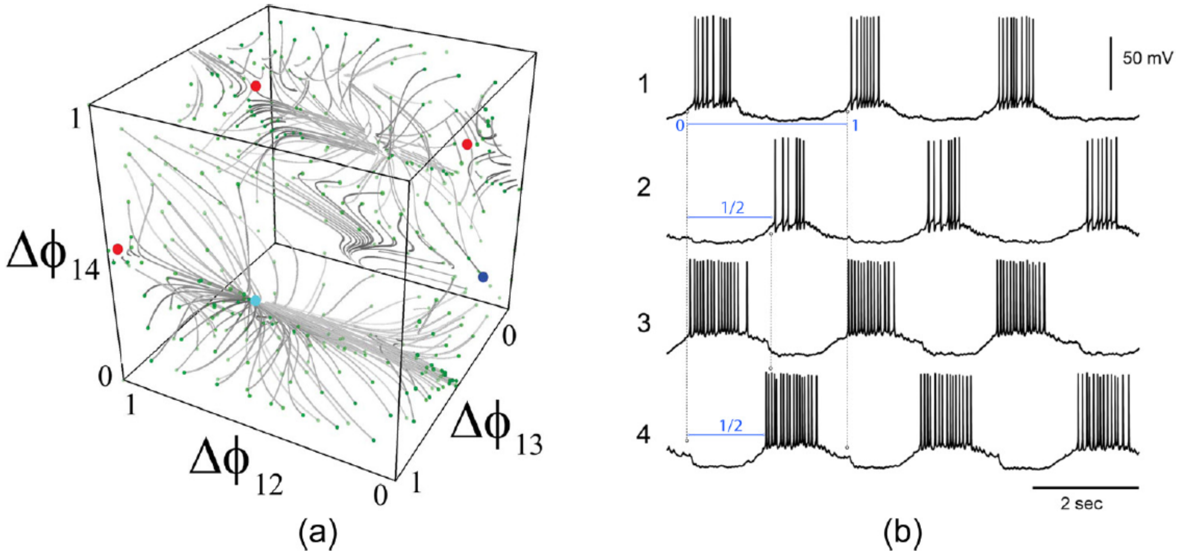

Figure 1.5: (a) Phase space of the network withe the fixed phase shifts. (b)Network bursting recorded from Si1s and Si2s during the swimming activity. Recordings provided courtesy of A. Sakurai. [27]

robustness of the rhythm. Later studies revealed that the cells are not bursters in isolation. They are tonic spiking or hyperpolarized quiescent cells in isolation. Also, the experimental studies showed that the phase locked rhythm generation is not the only feature of the network. Many different characteristics of the network were identified and these characteristics are discussed in the later chapters. In this study, we will use a more detailed and biologically plausible mathematical model to investigate the underlying mechanism of the Melibe swim CPG.

1.3 Purpose of The Study

In this study, we use a highly detailed and biologically plausible Hodgkin-Huxley type conductance base model to understand the underlying mechanism of rhythm generation in the swim CPGs of sea slugs. The interest to this area is motivated by the common dynamic properties of various neural systems including motion (sensory and network level) and control mechanisms in invertebrates, mammals, as well as humans. Many abnormal neurological phenomena are underpinned by perturbations of normal mechanisms that govern behaviors. There is emerging evidence that more advanced invertebrates and vertebrates have even a common design of forebrain circuits in embryonic brain structures of mammals.

The simplicity of invertebrate CPGs provide the opportunity for model studies for understanding and analyzing the principles of the rhythm generation. The complexity level of vertebrate and invertebrate neuronal circuits are not comparable but the similar features of both animal types and studies on the invertebrate CPGs can provide an insight into the more complex networks.

The general theme of this study, mathematical principles of complex rhythms in biology will bring new dimensions to research conducted in computational and experimental neuroscience. The methodology and computation technology that we develop will be a tool for future scientists, helping researchers with less expertise in computational sciences to create biologically plausible and models faster and more accurately. It is imperative to devise tractable, data-driven/assimilated models for integrating theoretical and experimental neuroscience. The knowledge and the tools created by this project will ultimately lead to new approaches to re-wiring or rebalancing disordered networks. It will also inform treatment of neurological disorders that emerge when larger-scale interactions within the circuits of the brain are disrupted such as stroke, and traumatic brain or spinal cord injury. This study will also provide a powerful substrate for hypothesis testing relating to elucidating the mechanisms involved in mental health disorders.

The possible technology impacts of the project include informing treatment and diagnosis of mental illnesses and neurological conditions relating to motor pattern generation; informing the engineering of better prosthetics; developing CPG based robots with bio-inspired locomotion principles.

CHAPTER 2

LATENT PARABOLIC BURSTERS AND FAST THRESHOLD MODULATIONS

2.1 Introduction

The neurons in the nervous system form highly complex networks, and central pattern generators (CPGs) are a commonly seen circuitry in the central nervous system. CPGs are small neuronal circuits which can autonomously generate rhythmic activity when activated and are responsible for vital rhythmic behavior like the heartbeat, respiration, walking, breathing, swallowing, flying and swimming. Emergent collaborative studies between experimentalist and computational researchers promote the unity of the concept that both invertebrate and vertebrate animals share similar formations and mechanism. Therefore, to understand more complex structures like the mammal and human nervous system, it is essential to understand more basic circuits in more simple animals.

The CPGs of invertebrates are simpler compared to more complex animals like mammalians and easier to run experimental studies. Sea slugs are useful subjects in this kind of studies. The simplicity of their CPGs and also similarities to CPGs of more complex animals make them highly convenient for experimental studies. The complexity level of invertebrates and mammals is not comparable but understanding simple CPGs of this primitive animals provide an insight into working mechanisms of more complex animals like mammals and human. The mostly studied sea slugs are *Tritonia, Aplysia, Dendronotus, Clione, Lymnaea* and *Melibe.* In this study, we will look at insights of rhythm generation mechanism of Melibe

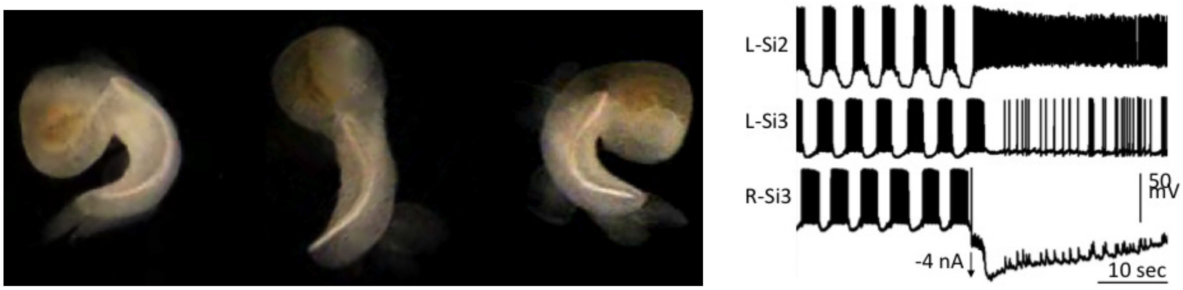

(a) (b)

Figure 2.1: (a) Melibe leonina lateral swim style. (b) Network bursting in swim interneurons (Si) of the Melibe swim CPG halts when Si3R is hyperpolarized, thus its counterpart Si3L begins tonic spiking; the photographs and in-vitro recording provided courtesy of A. Sakurai [30]

swim CPG in fine details. [37]. The circuitry is shown in Fig. 2.2(a) depicts only some core elements identified in the biological CPG; its detailed diagram can be found in [30].

Rhythm generation can occur at cellular level or network level. To understand, underlying rhythm generation mechanism in these neuronal circuits, a variety of mathematical models are developed. Despite the extensive work in this area, how CPGs work remains unclear. Understanding the rhythm generation mechanism of small and simple circuits is the first step of understanding more advanced structures.

Being inspired by experimental studies of voltage activity recorded from the swim CPGs of the sea slugs *Melibe leonina* and *Dendronotus iris*, we would like to develop an assembly line for CPG construction made of coupled biophysically plausible models. Our first simplifying assumption is that CPGs are made of universal building blocks – half-center oscillators (HCOs) [38]. Loosely speaking, an HCO is treated as a pair of interneurons interacting with each other through reciprocally inhibitory synapses and exhibiting anti-phase bursting. The interneurons of an HCO can be endogenous bursters, tonic spiking or quiescent ones, which

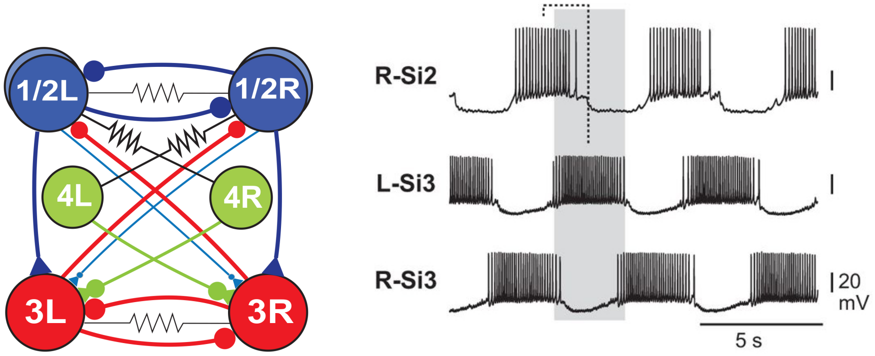

(a) (b)

Figure 2.2: (a) A core circuitry of the biological Melibe swim CPG with inhibitory (●), excitatory (◄) and electrical (\/\/) synapses [30]. (b) In-vitro voltage activity recordings from identified swim interneurons, Si2R and Si3L/R, of the Melibe swim CPG with the characteristic $\frac{3}{4}$ -phase lag between the HCO2 and HCO3; intracellular recording provided courtesy of A. Sakurai [30].

exhibit alternating bursting only when they inhibit each other. Theoretical studies [39] have indicated that formation of an anti-phase bursting rhythm is always based on slow subsystem dynamics. There are three basic mechanisms to generate alternating bursting in the HCO: release, escape, and post-inhibitory rebound (PIR). The first mechanism is typical for endogenously bursting neurons [40, 41]. The other two mechanisms underlie network bursting in HCOs comprised of neurons, which are hyperpolarized quiescent in isolation [42, 43, 44, 45]. Our second assumption is that the swim CPG interneurons are intrinsic tonic spikers that become network bursters only when externally driven or coupled by inhibitory synapses, as recent experimental studies suggest [30]. The third assumption is that network bursting in the *Melibe* swim CPG is *parabolic*, i.e., the spike frequency within a burst increases at the middle, and decreases at the ends, as one can observe from Fig. 2.3. This observation indicates the type of neuronal models to be employed to describe network cores. Our model of choice for parabolic bursting is the Plant model [46, 47, 48]. The

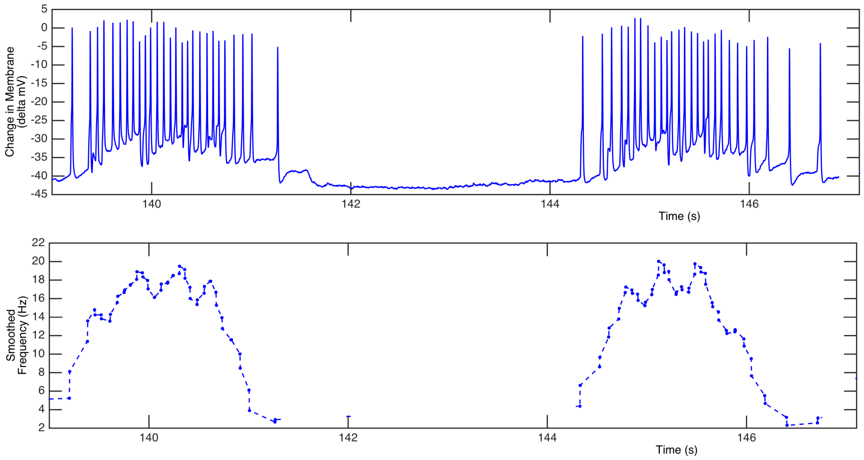

Figure 2.3: (a) Parabolic distribution of spike frequency within bursts produced by networked interneurons in the Melibe swim CPG. Recording provided courtesy of A. Sakurai and time series analysis by A. Kelley.

Plant model has been developed to accurately describe the voltage dynamics of the R15 neuron in a mollusk *Aplysia californica*, which has turned out to be an endogenous burster [49]. Most dynamical properties of the R15 neuron have been modeled and studied in detail [50, 51, 52, 53, 54, 37].

2.2 Methods: the Plant model of parabolic bursting

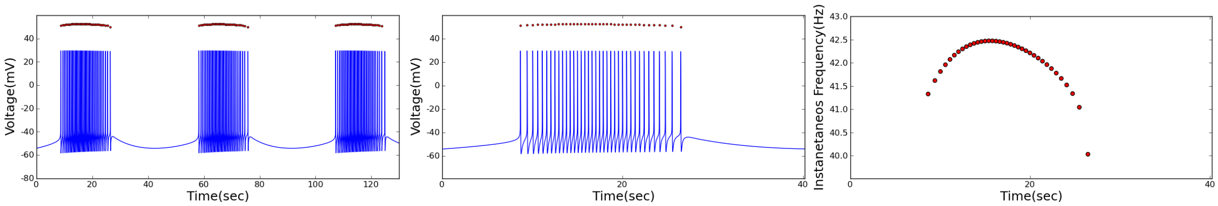

(a) (b) (c)

Figure 2.4: (a) Endogenous bursting in the Plant model as alternations of tonic spiking activity and quiescent periods. (b) Single burst featuring a characteristic spike frequency increase in the middle of each burst. (c) Parabolic shape of the frequency distribution of spikes within a burst is a feature of this kind of bursting. The parameters are $\rho = 0.00015 ms^{-1}$, $K_c = 0.00425 ms^{-1}$ and $\tau_x = 9400 ms$.

The conductance based Plant model [48] for the R15 neuron [54] located in the abdominal ganglion of a slug *Aplysia Californica* is given by the following set of ordinary differential equations derived within the framework of the Hodgkin-Huxley formalism to describe the dynamics of the fast inward sodium [Na], outward potassium [K], slow TTX-resistant calcium [Ca] and an outward calcium sensitive potassium [KCa] currents.The fast subsystem is given by the equations below:

$$C_m\dot{V} = -I_{Na} - I_K - I_{Ca} - I_{KCa} - I_{leak} - I_{ext} - I_{syn}, \tag{2.1}$$

$$(I_{Na} = g_{Na}m_\infty^3(V)h(V - V_{Na}), \quad I_K = g_K n^4(V - V_K), \tag{2.2}$$

$$I_{Ca} = g_{Ca}x(V - V_{Ca}), \quad I_{KCa} = g_{KCa}\frac{[Ca]_i}{0.5 + [Ca]_i}(V - V_K), \tag{2.3}$$

$$I_{leak} = g_L(V - V_L), \quad I_{syn} = \frac{g_{syn}(V_{post} - E_{rev})}{1 + e^{-k(V_{pre} - \Theta_{syn})}}), \tag{2.4}$$

$$\dot{n} = \frac{n_\infty(V) - n}{\tau_n(V)}, \quad \dot{h} = \frac{h_\infty(V) - h}{\tau_h(V)} \tag{2.5}$$

The last three currents are the generic ohmic leak I_{leak}, external constant I_{ext} and synaptic I_{syn} currents flowing from a pre-synaptic neuron. The full details of the representation of the currents employed in the model are given in the Appendix A.

There are two bifurcation parameters in the individual cell model. The first one is the constant external current, I_{ext}, which is set $I_{ext} = 0$. Following [55], the other bifurcation parameter, Δ_1, is introduced in the slowest equation Ca where the slow subsystem is :

$$\dot{Ca} = \rho \left(K_c x (V_{Ca} - V + \Delta_1) - Ca \right), \tag{2.6}$$

$$\dot{x} = ((1/(e^{0.15*(-V-50)} + 1)) - x)/\tau_x, \tag{2.7}$$

describing the concentration of the intracellular calcium in the Plant model. By construction, Δ_1 is a deviation from a mean value of the reversal potential $V_{Ca} = 140mV$ evaluated experimentally for the calcium current in the R15 cells. As such, this makes Δ_1 a bifurcation parameter. Secondly its variations are not supposed to alter the topology of the slow motion manifolds in the 5D phase space, which are called tonic spiking and quiescent in the mathematical neuroscience context, as they are made of, respectively, round periodic orbits and equilibrium states [of the slow subsystem] of the model (Fig. 2.5).

At $\Delta_1 = 0$, the neuron is an endogenous burster, see Fig. 2.4. According to [56], this type of bursting is termed *parabolic.* The reason for this term is that the spike frequency within bursts is maximized in the middle of bursts and minimized at the beginning and the end (see Fig. 2.4c). The parabolic structure of a burst is due to the calcium-activated potassium current. Its magnitude is determined by the intracellular calcium concentration. As the intracellular calcium concentration increases, the calcium-dependent potassium current gets activated, which causes an increase of the inward potassium current. As the membrane potential increases over a threshold value, the intracellular calcium concentration decreases, as well as the outward potassium current (see Eq. (20) in the Appendix). The parabolic distribution of spikes within bursts is shown in Fig. 2.4. The instant frequency value is calculated by the reciprocal of each inter-spike interval. Panels b and c of Fig. 2.4 disclose the parabolic inter-spike structure of bursts.

It was shown in [56] that the mechanism underlying a transition between quiescent and tonic spiking of bursting in the Plant model is due to a homoclinic bifurcation of a saddle-node equilibrium state [57, 58]. This bifurcation occurs in the fast 3D (V, h, n)-subspace of the model and is modulated by the 2D slow dynamics in the (Ca, x)-variables, which are determined by slow oscillations of the intracellular calcium concentration [46, 47]. The unfolding of this codimension-one bifurcation includes an onset of a stable equilibrium, which is associated with a hyperpolarized phase of bursting, and on the other end, an emergent stable periodic orbit that is associated with tonic spiking phase of bursting. The period

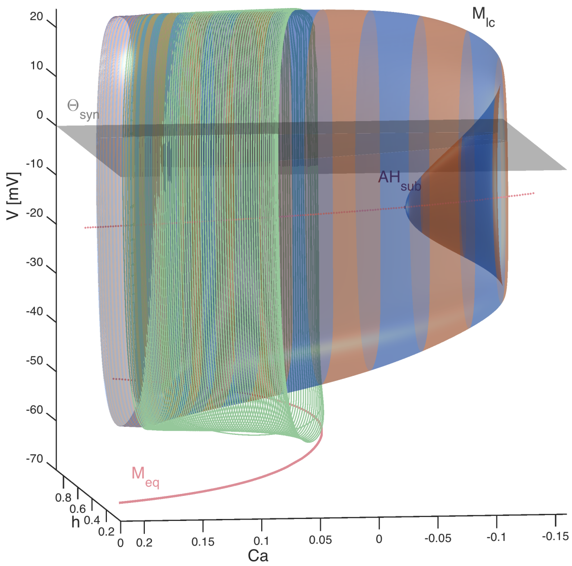

Figure 2.5: Bursting (green) orbit recursively switching between two slow–motion critical manifolds: tonic spiking, M_{lc}, with a characteristic fold and originating through a sub-critical Andronov-Hopf (AH) bifurcation from a depolarized equilibrium state, and quiescent, M_{eq} (orange curve), projected onto the (h, V) and slow Ca variables of the of the Plant model; a plane represents the synaptic threshold, $\Theta_{syn} = 0mV$.

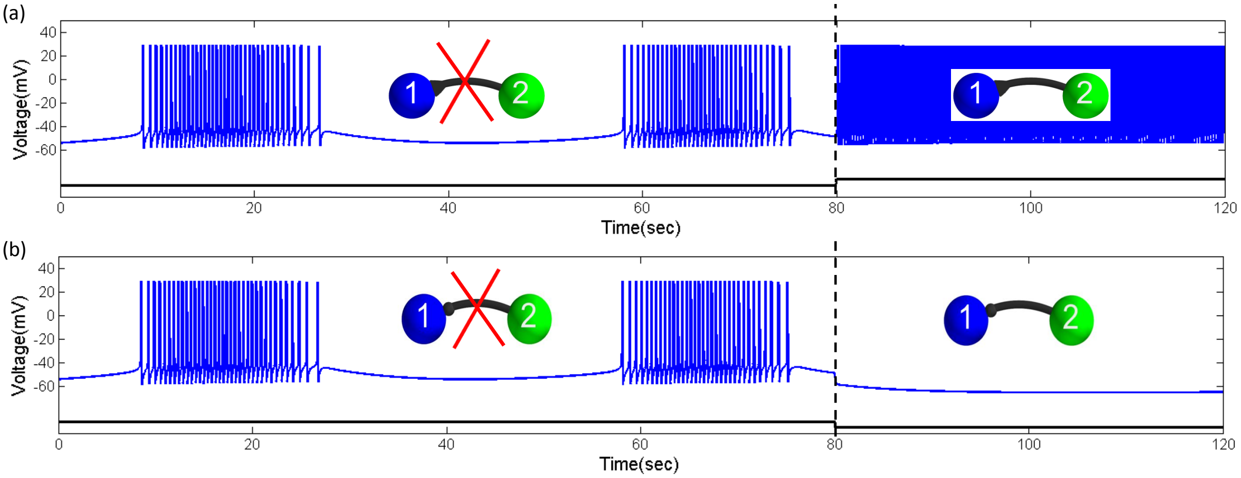

Figure 2.6: Responses of the bursting neuron ($\Delta_1 = 0mV$) on the synaptic drive $I_{syn} = g_{syn}(V - V_{rev})$. (a) Excitatory synaptic drive with $g_{syn} = 0.002nS$ and $V_{rev} = 40mV$ applied at $t = 80sec$ switches the neuron from bursting to tonic spiking activity. (b) The inhibitory drive with $g_{syn} = 0.005nS$ and $V_{syn} = -80mV$ halts bursting and makes the neuron hyperpolarized quiescent.

of this stable orbit decreases, as it moves further away from the saddle-node equilibrium mediated by decreasing calcium concentration. The period of the tonic spiking orbit grows with no upper bound as it approaches the homoclinic loop of the saddle-node [59].

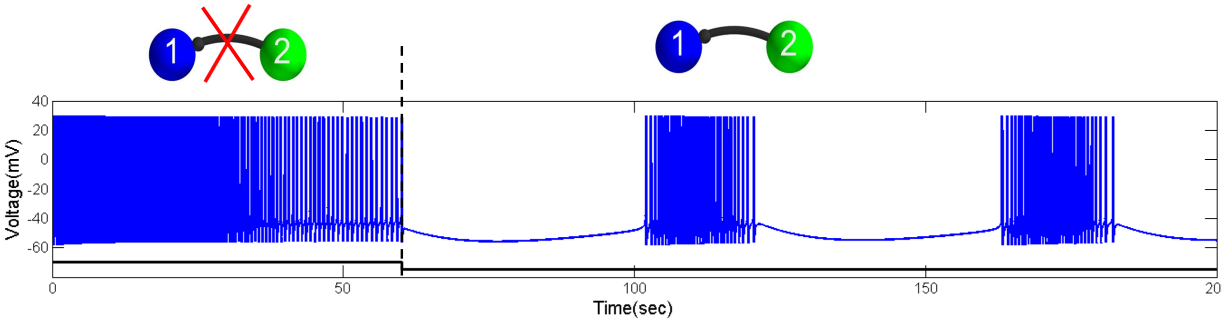

Figure 2.7: Tonic spiking neuron 1 at $\Delta_1 = -34mV$ near the bifurcation transition between tonic spiking and bursting is forced to become a network burster with an application of an inhibitory drive with $g^{inh}_{syn} = 0.001nS$, from the pre-synaptic neuron 2 at $t = 60sec$. Halting the inhibitory drive restores tonic spiking activity in the targeted neuron (not shown).

Variations of Δ_1 change the duty cycle of bursting, which is a ratio of the active tonic spiking phase of bursting to its period. Decreasing Δ_1 reduces the inactive, quiescent phase of bursting, i.e. increases its duty cycle. Zero duty cycle is associated with the homoclinic saddle-node bifurcation that makes the neuron hyperpolarized quiescent. This corresponds to an emergence of stable equilibrium state for all dynamical variables of the model (3.1). In other words, decreasing Δ_1 makes the active phase longer so that below a threshold $\Delta_1 = -32mV$ the neuron switches to tonic spiking activity. Tonic spiking activity is associated with the emergence of a stable periodic orbit in the fast (V, h, n)-subspace, while the (Ca, x)-variables of the slow subspace converge to a stable equilibrium state. As such, bursting occurs in the Plant and similar models due to relaxation of periodic oscillations in the 2D (Ca, x)-subspace, which slowly modulates fast tonic spiking oscillations in the (V, h, n) variables. The relaxation limit cycles emerge from one and collapse into the other equilibrium state in the (Ca, x)-plane through Andronov-Hopf bifurcations, which can be sub- or super-critical. At the transitions between bursting and tonic spiking, and bursting and hyperpolarized quiescence, the neuron can produce chaotic dynamics, which are basically due to the membrane potential oscillatory perturbations of plain canards at the folds of the relaxation cycle.

2.3 Endogenous and network bursting. Inhibitory and excitatory drives

A half-center oscillator is a network of two neurons coupled by reciprocally inhibitory synapses that robustly produce bursting in alternation or anti-phase bursting. Such a network can be multistable, i.e., produce other bursting rhythms as well, such as synchronous

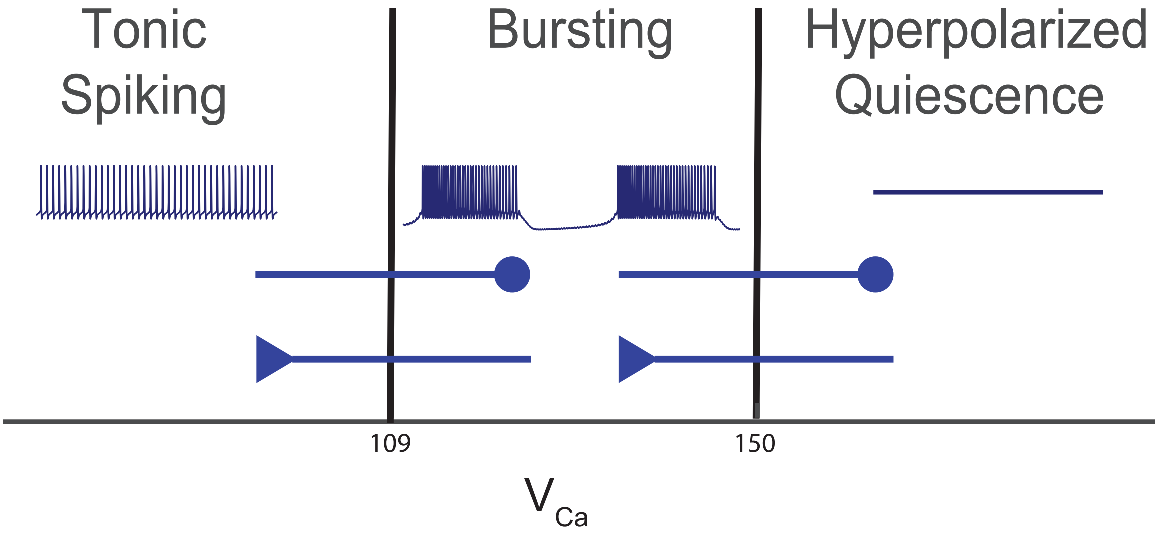

Figure 2.8: Bifurcation diagram of the isolated Plant model. As the bifurcation parameter V_{Ca} *increases, the isolated cell switches states between tonic spiking to bursting and bursting into hyperpolarized quiescent. Also, the transition between the states is possible through the synapses. These transitions are also indicated in the diagram. Applying inhibition to tonic spiking cell results in a burster cell and further inhibition pushes the cell into the hyperpolarized quiescent state. The bifurcation diagram summarizes Figs 2.6 and Fig 2.7.*

bursting [40] and rhythmic outcomes with slightly shifted phase lags between the endogenously bursting neurons [41].

In this study, the synaptic current I_{syn} is modeled through the fast threshold modulation (FTM) approach [60]. The synapses are assumed to be fast and non-delayed, which is true for the swim CPG in both sea slugs under consideration. The synaptic current is given by

$$I_{syn} = g_{syn}(V_{post} - E_{syn})\frac{1}{1 + e^{-k(V_{pre} - \Theta_{syn})}}, \tag{2.8}$$

where g_{syn} is the maximal conductance of the current, which is used as a bifurcation parameter of the networked model; $V_{post}(t)$ and $V_{pre}(t)$ are the voltages on the post-synaptic (driven) and pre-synaptic (driving) neurons; E_{syn} is the synaptic reversal potential. To make I_{syn} excitatory, we set $E_{syn} = 40mV$, while in the inhibitory case we set $E_{syn} = -80mV$. In

Eq. (2.8), the second term is a Boltzmann coupling function that quickly, ($k = 100$), turns the synaptic current on and off as soon the voltage, V_{pre}, of the (driving) pre-synaptic cell(s) raises above and falls below the synaptic threshold, here $\Theta_{syn} = 0mV$ (Fig. 2.5).

To model the constant synaptic drive onto the post-synaptic neuron, we assume that $V_{pre} > \Theta_{syn}$. This allows us to calibrate the state of the post-synaptic neuron, and to determine the drive threshold that separates the qualitatively distinct states of the individual and networked neurons. This statement is illustrated in Fig. 2.6 by simulating responses of the endogenous parabolic burster to network perturbation. Figure 2.6(a) shows, with a properly adjusted excitatory drive, that the endogenous burster switches into tonic spiking activity. On the other hand, bursting in the networked neuron can be halted when it receives a sufficient inhibitory drive from the pre-synaptic neuron of the network (Figure 2.6(b)). Eliminating either drive makes the post-synaptic neuron return to its natural state, i.e., these experiments *de-facto* prove that the neuron is mono-stable for the given parameter values.

An HCO, in the canonical Brown definition [36], is a pair of neurons bursting in anti-phase when they are networked by inhibitory synapses. In isolation, such neurons are not endogenous bursters but tonic spikers instead, or remain quiescent [3]. There are multiple mechanisms underlying such anti-phase bursting, or, more accurately, anti-phase oscillations in HCOs and CPGs made of relaxation oscillators [45, 61]. The list includes the well-studied mechanisms of post-inhibitory rebound and escape for quiescent neurons [42, 39, 43, 62, 63], as well as less-known mechanisms of HCOs constituted by intrinsically spiking neurons. Such

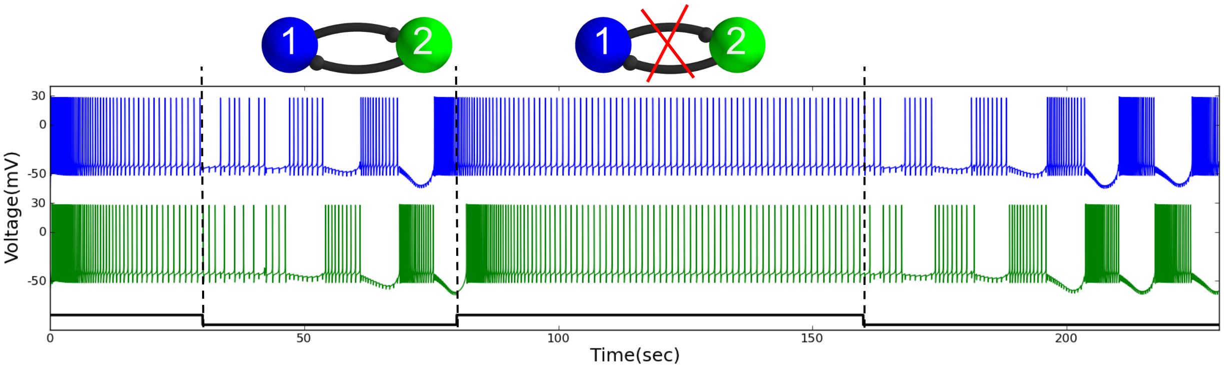

Figure 2.9: Anti-phase network bursting produced by a HCO of two Plant neurons as soon as the inhibition is turned on. Blocking the inhibition restores tonic spiking activity in both neurons, and vice versa. Here, the the network parameters are $g_{syn}^{inh} = 0.008nS$ *and* $E_{syn} = -80mV$*, and the parameters of the individual neurons are the following:* $\Delta_1 = -60mV, \rho = 0.0003ms^{-1}$, $K_c = 0.0085ms^{-1}$, $\tau_x = 235ms$ *and* $x_\infty(V) = 1/(1 + e^{-0.15(V+50)})$.

networks utilizing the Plant models are discussed below.

To construct such an HCO with relatively weak inhibitory coupling, the Plant model must be first set into the tonic spiking mode. This is done by setting the bifurcation parameter, $\Delta_1 = -34mV$, see Fig. 2.7. Next, we consider a unidirectional network where the tonic spiking neuron 1 starts receiving an inhibitory drive of $g_{syn} = 0.001nS$ from the post-synaptic neuron 2 at $t = 60sec$. The inhibitory drive is sufficient to shift the post-inhibitory neuron over the bifurcation transition back into bursting activity. The minimal inhibitory drive must be increased proportionally to make the targeted neuron a network burster whenever it stays further away from the bifurcation transition between tonic spiking and bursting in isolation.

2.4 Forming a half-center oscillator

In this section, we discuss the dynamics of half-center oscillators made of two tonically spiking Plant neurons reciprocally coupled with inhibitory synapses. As before, we describe such synapses within the framework of the fast threshold modulation (FTM) paradigm using Eq. (2.8) to match the shape and magnitude of inhibitory postsynaptic potentials (IPSPs) in the post-synaptic neurons. IPSPs are the indicators of the type and the strength of synapses in the network.

We perform simulations in a fashion that is analogous to the dynamic clamp technique used in neurophysiological experiments. Dynamic-clamp is an electrophysiology method which is used for simulating dynamic biological features such as membrane potential and synaptic currents in between living cells [64, 65, 66]. The approach involves the *dynamic* block, restoration and modulation of synaptic connections during simulation. These modeling perturbations should closely resemble the experimental techniques of a drug-induced synaptic blockade, modulation, wash-out, etc. Restoring the chemical synapses during a simulation makes the HCO regain network bursting activity with specific phase characteristics. Depending on the coupling strength as well as the way the tonically spiking neurons are clamped, the network bursting may change phase-locked states, i.e., be potentially multistable. Experimental observations also suggest specific constraints on the range of coupling strengths of the reciprocal inhibition, such that the networks stably and generically achieve the desired phase-locking.

Figure 2.9 demonstrates the stages of anti-phase bursting formation in the HCO. The

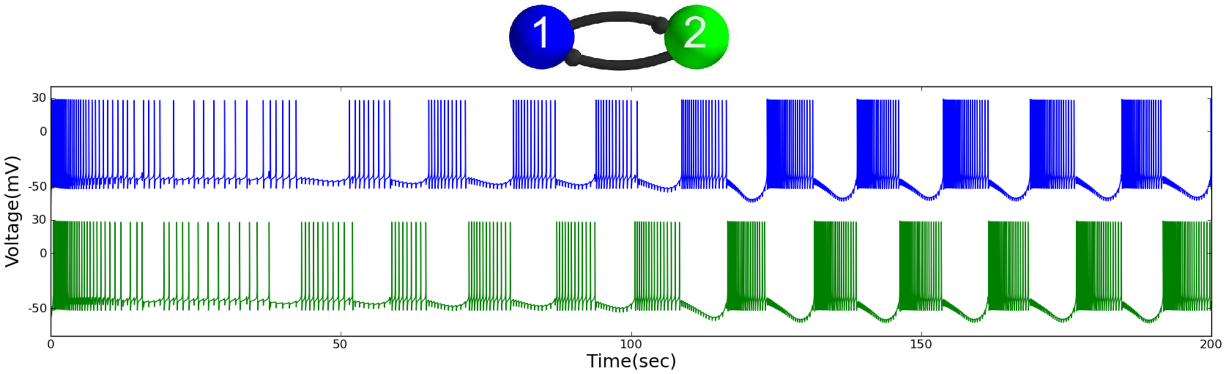

Figure 2.10: Onset of emergent network anti-phase bursting in the HCO with reciprocally inhibitory.($E_{syn} = -80mV$*) synapses at* $g_{syn}^{inh} = 0.0073nS$*.*

uncoupled neurons are initiated in tonic spiking mode. After turning on the reciprocally inhibitory synapses $g_{syn} = 0.008nS$, the HCO quickly transitions to the regime of robust anti-phase bursting. Turning off the synapses restores the native tonic spiking activity in both neurons. Turning on the reciprocal synapses makes the HCO regain the network bursting. Note that the length of transients from tonic spiking to network bursting depends on the strength of the synaptic coupling for the fixed parameters of the individual Plant neurons. By comparing the magnitude of IPSPs in the voltage traces represented in Figs. 2.9 and 2.10, one can conclude that the coupling in the later case is weaker. This is why the onset of network bursting in the HCO is less pronounced.

Our modeling studies agree well with experimental recordings from the identified interneurons in the *Melibe* swim CPG which suggests that the observed bursting is due to synergetic interactions of interneurons of the network [30]. One can see from Fig. 2.1(b) that network bursting in the biological HCO formed by two Si3 interneurons of the *Melibe* swim CPG is seized as soon as the right one, Si3R, receives a negative current pulse that makes it hyperpolarized quiescent, while its left bursting counterpart, Si3L, turns into tonic spiking activity instead. Moreover, one can deduct from the wiring diagram of the CPG depicted in Fig. 2.2(a) and the analysis of voltage traces represented in Fig. 2.1(b) that the interneuron Si2L becomes a tonic-spiker as soon as the pre-synaptic interneuron Si3R stops inhibiting it (compare with Fig. 2.9.) This further supports the assertion that the swim CPG is made of intrinsically tonic spiking interneurons.

To test the robustness of network anti-phase bursting to perturbation and to calibrate the necessary influx of reciprocal inhibition generated by the Plant neurons, we consider an HCO with excitatory autapses. The objective here is to determine an equivalent amount of excitatory drive to be projected onto the post-inhibitory network burster to cancel out the inhibitory drive and shift it back to the initial tonic-spiking mode.

An autapse is a synapse of a neuron onto itself, where the axon of the neuron ends on its dendrite. After their discovery [67] autapses have been observed in a range of nervous systems. The autapses are arguable to be responsible for tuning of neural networks. This

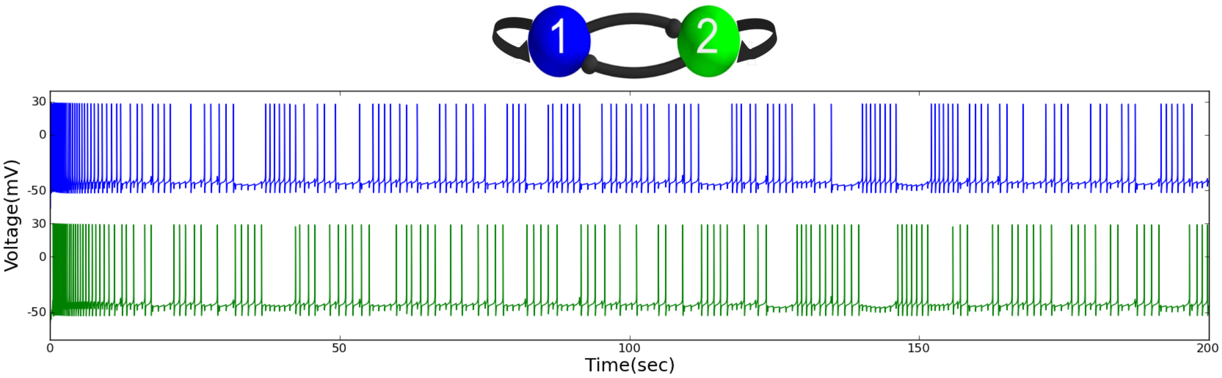

Figure 2.11: Turning on the excitatory autapses at $g_{aut}^{exc} = 0.016nS$ *in the HCO with* $g_{syn}^{inh} = 0.0073nS$ *halts pronounced network bursting.*

particular configuration of the HCO depicted in Fig. 2.11 is formally motivated by the swim CPG circuitry, see Fig. 2.2(a). One can see from it that the interneurons of the bottom HCO receive excitatory drives from the top interneurons forming the top HCO. We would like to find the threshold over which the neurons no longer form a stably bursting HCO. This would allow us to calibrate and quantify the relative strengths of the mixed synaptic connections in the swim CPG models.

In this HCO configuration, each neuron inhibits its counterpart and self-excites through the autapse. Both autapses are introduced to the model using the FTM approach with $E_{aut} = 40mV$. In this experiment, the conductance values for inhibitory synapses are set at $g_{syn}^{inh} = 0.0073nS$. This is sufficient for the HCO to generate robust anti-phase bursting as seen in Fig. 2.10. Next, we add the autapses along with inhibition and gradually increase g_{aut}^{exc}. We found that increasing g_{aut}^{exc} proportionally increase the delay. At $g_{aut}^{exc} = 0.016nS$, the network stops exhibiting anti-phase bursting. We note that unlike a permanent excitatory drive from pre-synaptic neurons, an introduction of the excitatory autapse, acting only when the self-driving neuron is above the synaptic threshold, is effectively perturbation equivalent for the calibration purpose.

2.5 Assembly line of a *Melibe* swim CPG

In this final section, we put together a pilot model of the Melibe swim CPG according to a circuitry based on identified interneurons and synapses; its wiring diagram is sketched in Fig. 2.2(a). This network model is made of the two HCOs constituted by tonic spiking Plant

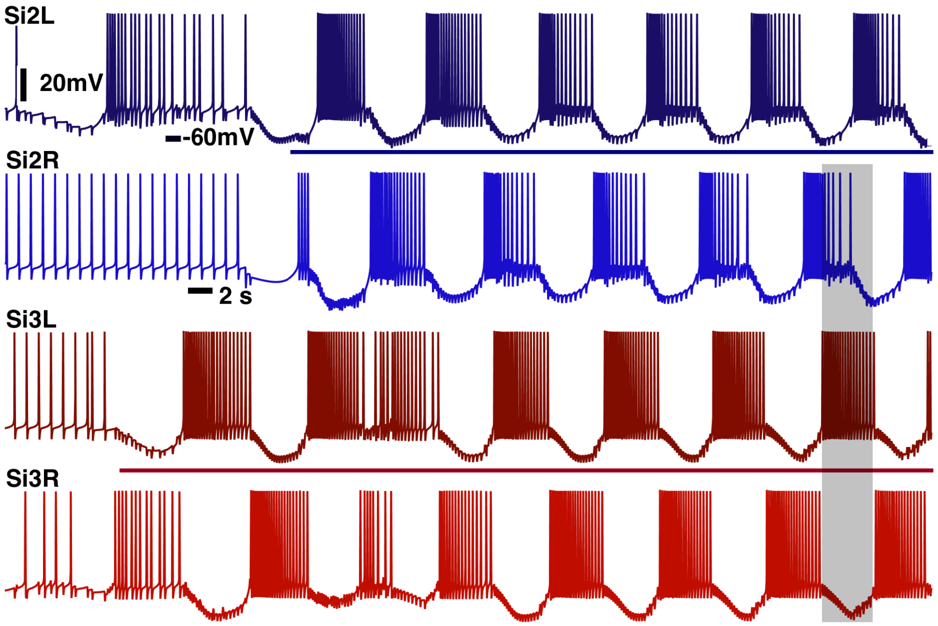

Figure 2.12: Assembly line of the Melibe swim CPG model out of four intrinsically tonic spiking Plant neurons. First, the reciprocal inhibition between Si3R and Si3L is turned on, followed by turning on the reciprocal inhibition between Si2R and Si2L, and next simultaneous turning on unidirectional cross-lateral inhibition from Si3R(L) projected onto Si2L(R), and bi-lateral excitation originating from Si2R(L) down onto Si3R(L). After a short transient, the CPG model exhibits the desired 3/4 phase shift lag between Si2L and Si3L. Compare with voltage traces of the biological CPG in Fig. 2.2(b).

neurons. We would like to find out whether this sample CPG model can already produce phase lags similar to those between bursting interneurons in the biological CPG. For the sake of simplicity, we do not include Si4R/L interneurons in the model, and we also omit electrical synapses. It is known from experimental studies [30] that blocking chemical, inhibitory and excitatory synapses between the interneurons may be sufficient to break down the motor pattern by the network. Figure 2.2(b) points out that the interneurons of either HCO burst in anti-phase and there is the characteristic 3/4 phase lag between the burst initiation in the neurons Si2L and Si3L, as well as between Si2R and Si3L. This phase lag is repeatedly observed in both adult and juvenile animals.

As before, we use the Plant neurons initiated in the tonic spiking mode, relatively close to the transition to bursting. Initial conditions of the neurons are randomized. After letting the neurons settled down to tonic spiking activity, the network connections are turned on. As Fig. 2.12 shows, with the reciprocal inhibition being first turned on, the bottom interneurons Si3L and Si3R become anti-phase network bursters, and so do Si2R and Si2L as soon as the reciprocal inhibition between them is turned them on, too. At this stage, the CPG model is formed by two uncoupled HCOs. A few seconds later, they become coupled by simultaneous turning on the unidirectional cross-lateral inhibition from Si3R(L) projected onto Si2L(R), and bi-lateral excitation from Si2R(L) down onto Si3R(L). One can see from this figure that all four interneurons of the CPG model exhibit network bursting with the desired phase lags. These are 0.5 (half period) between the interneurons of each HCO, and 3/4 (a fraction of the network period) between the HCOs, or between the corresponding reference interneurons Si2L and Si3L. We note that such a phase shift was reported in a similar *Melibe* swim CPG constituted by endogenous bursters; that model also incorporated electrical synapses [27]. There is a great room for improvement of CPG network models to include other identified interneurons and to incorporate additional electrical synapses to find out whether additions of new elements can stabilize or desynchronize the desired bursting pattern as it was done using the Poincaré return maps for endogenous bursters [22]. Of our special interest are various problems concerning structural stability of the network, and its robustness (Lyapunov stability) for bursting outcomes subjected to perturbations by pulses of the external current, as well as reductions to return maps between burst initiations in constituent neurons. These questions are beyond the scopes of the given examination and will be addressed in full detail in our forthcoming publications soon. The question about a possible linking of the characteristic $\frac{3}{4}$ phase lag and the *Melibe leonina* lateral swim style is the paramount one among them.

2.6 Summary

We have discussed a basic procedure for building network bursting CPGs made of intrinsically tonic spiking neurons. As a model for such networks, we have employed the biophysically plausible Plant model that was originally proposed to describe endogenous bursting R15-cells in the *Aplysia* mollusk. Such bursting was intracellularly recorded, and identified as parabolic, from the known interneurons in the swim CPGs of two sea slugs: *Melibe leonina* and *Dendronotus iris*. There is experimental evidence that bursting in these swim CPGs is due to synergetic interactions of all constituent neurons that are intrinsic tonic-spikers in isolation. To model the *Melibe* swim CPG, we have first examined dynamical and structural properties of the Plant model and its responses to perturbations. These perturbations include inhibitory and excitatory inputs from pre-synaptic neurons in the network. We have identified the transition boundary beyond which the bursting Plant model became a tonic-spiker and shifted it slightly over the threshold using an introduced bifurcation parameter. We have shown that the perturbed/calibrated Plant neuron, exhibiting intrinsically tonic spiking activity, becomes a network burster when it receives an inhibitory drive from a pre-synaptic neuron. By combining two such neurons, we have created a genuine half-center oscillator robustly producing anti-phase bursting dynamics. We have also considered an HCO configuration with two excitatory autapses to assess the robustness of anti-phase bursting with respect to excitatory perturbations. Finally, we have employed all necessary components to assemble a truncated model of the *Melibe* swim CPG with the characteristic 3/4-phase lags between the bursting onsets in the four constituent interneurons. In future studies, we plan to examine the dynamics of the CPG models with all synaptic connections, including electrical, as well as incorporating additionally identified interneurons. We will also explore their structural stability, robustness and potential multi-stability of their bursting outcomes with various phase lags. An additional goal is to find out whether the motor pattern with the 3/4-phase lags will persist in networks with interneurons represented by other mathematical models including phenomenologically reduced ones. Potentially, these findings shall provide a systematic basis for comprehension of plausible biophysical mechanisms for the origination and regulation of rhythmic patterns generated by various CPGs. Our goal is to extend and generalize the dynamical principles disclosed in the considered networks for other neural systems besides locomotion, such as olfactory cellular networks.

CHAPTER 3

DIFFERENT INTRINSIC CELL DYNAMICS AND SLOW SYNAPSES

3.1 Introduction

The Melibe swim CPG was initially thought to be a very simple neuronal circuit of two pairs of interneurons but recent studies on identifying Melibe swim CPG, reveals that four pairs of interneurons form the circuit [30, 27]. The *in vitro* voltage recordings gave perfect opportunity to create a highly detailed and biologically plausible mathematical model. In the previous chapter, we have used a Hodgkin-Huxley formalism model initially designed for R15 cells of *Aplysia Californica* which are intrinsic bursters. We used a similar approach to model the *Melibe* swim CPG. The main difference between two animals is the behavior of the cells in isolation. The swim interneurons(Sis) are known to be network bursters. In isolation, the cells are either quiescent or tonic spiker cells. The circuit consists of four pairs of swim interneurons (Sis) which are symmetrically located in the *Melibe* brain, and these pairs form half-center oscillators(HCOs) which are commonly seen structures in CPGs and constitutes the main framework of these small neuronal circuits. HCOs are microcircuits in which neurons are reciprocally coupled via inhibition and fire or burst in anti-phase.

Experimental results showed that the cells in the CPG are network bursters and non-bursters in isolation. In order to implement this result to the mathematical model, we eliminated the bursting state by using dynamical systems theory. More specifically, it is known that Si2s are tonic spiking cells in isolation and Si3s are tonic spiking cells or quiescent cells. The delays and phase shifts in the network rhythm implied that the HCO mechanism between Si2s and Si3s are different. As mentioned in the previous chapter, generations HCOs can follow three mechanisms: release, escape and post-inhibitory rebound(PIR). Our first assumption is that HCO mechanism for Si2s is escape, and Si3s is PIR. According to the first assumption, we set the intrinsic dynamics of the cells as hyperpolarized quiescent for Si3s and tonic spiking for Si2s.

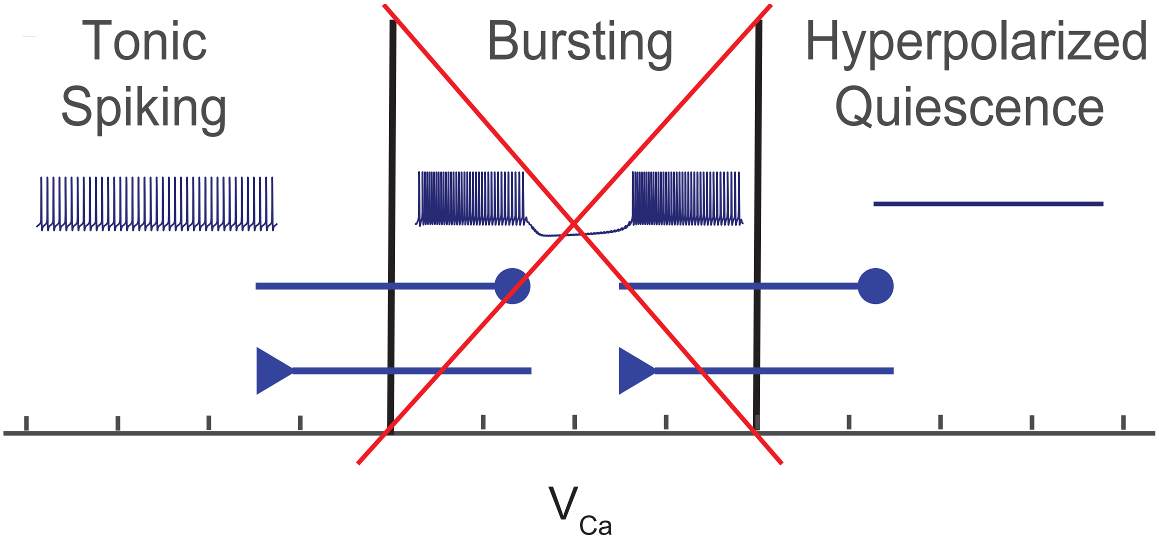

Figure 3.1: The mathematical model is calibrated to generate only tonic spiking and hyperpolarized quiescent activity. The bursting state is eliminated for $\Delta_2 = -2$*.*

Well designed neurophysiological experiments provided detailed information on the dynamics of synapses. Characteristics of synapses are implemented into the mathematical model through more advanced modeling methods. In the initial modeling study, FTMs were used to model synapses. In this chapter, FTMs are replaced by alpha synapses and dynamic synapses, which are biologically more plausible methods for synapse modeling.

For modeling, we used two experimental cases as reference: a control case where the animal is actively swimming and all connections are active and the curare case where the outgoing connections from Si3s are disabled by a synaptic blocker called d-tubocurarine. We started building our model by putting together the circuitry starting from curare case because it includes fewer connections compared to the control case and gives more insight into the characteristics of the existing synapses. After modeling the curare case correctly, we restored the blocked connections for control case. The essential features that we took into consideration during the modeling process were the difference in fundamental structures of the neurons, burst durations, delays in burst initiations and latency at the end of bursts.

3.2 Network

The details of the network will be explained in two subsections: biological network and mathematical network. In the biological network section, the original biological circuit and its features used in modeling are described. In the mathematical network section, the reduction process of the circuit for mathematical modeling is explained in details.

3.2.1 Biological Network

Identification of *Melibe* swim CPG is still an ongoing neurophysiological work. Details of the identification process and the circuit structure are given in the previous chapters. Briefly, the biological network consists of four pairs of swim interneurons (Si1, Si2, Si3, and Si4) and cells of each pair are located in contralateral parts of the brain (i.e., left and right). Each pair of Sis composes a simple HCO. The circuit retains excitatory and electrical synapses besides the inhibitory connections. Electrical connections exist between pairs of Si1s as well as Si2s. Also, there is a stronger electrical synapse between ipsilateral Si1s and Si2s on both sides of the brain. This feature will be used in circuit reduction process. Each synapse and cell in the CPG has its characteristics. Synapses can exhibit slow or fast dynamics. The cells differ in their activity in isolation as well as their neurophysiological properties. For instance, Si2s are the largest cells, so they are easier to detect in the brain. Other cells are smaller in size. Also, the inhibitory reversal potential varies depending on the physical size of the cell. Reversal potentials of Si2s and Si3s are $V_{Si2} = -80mv$ and $V_{Si3} = -50mv$.

As mentioned before, the studies on identifying Melibe swim CPG is an ongoing work. The circuit used in the previous chapter is slightly changed due to the newer experimental findings. In the previous model, we used contralateral excitation and ipsilateral inhibitions between Si2s and Si3s. Current experiments showed that the synapses from Si2s to Si3s are contralateral excitation and ipsilateral inhibition. The difference between the circuits is presented in Fig.3.2.

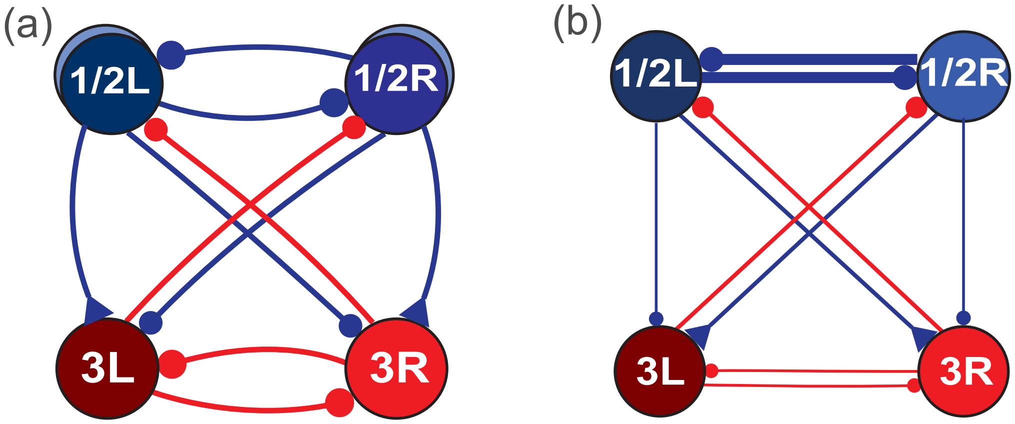

Figure 3.2: (a) Previously used simplified Melibe swim CPG where the synapses from Si2s to Si3s are contralateral inhibition and ipsi-lateral excitation. (b) The most recent simplified Melibe swim CPG where the synapses from Si2s to Si3s are contralateral excitation and ipsi-lateral inhibition.

Intracellular voltage values are recorded in saline where all synaptic connections are active (control case), and the outgoing connections from Si3s are blocked by the synaptic blocker curare (curare case). The circuit motifs for control and curare cases are shown in Fig. 3.3(a) and Fig. 3.4(a). Blocking the outgoing connections from Si3s which are reciprocal inhibitory connections between Si3s and the contralateral inhibitory connections from Si3s to Si2s, has a significant effect on the bursting characteristics of the network. Blockage of these synapses causes a significant increase in the burst duration. In control case, the burst length in average is around 2-4 seconds while it is around 12-13 seconds in curare case.

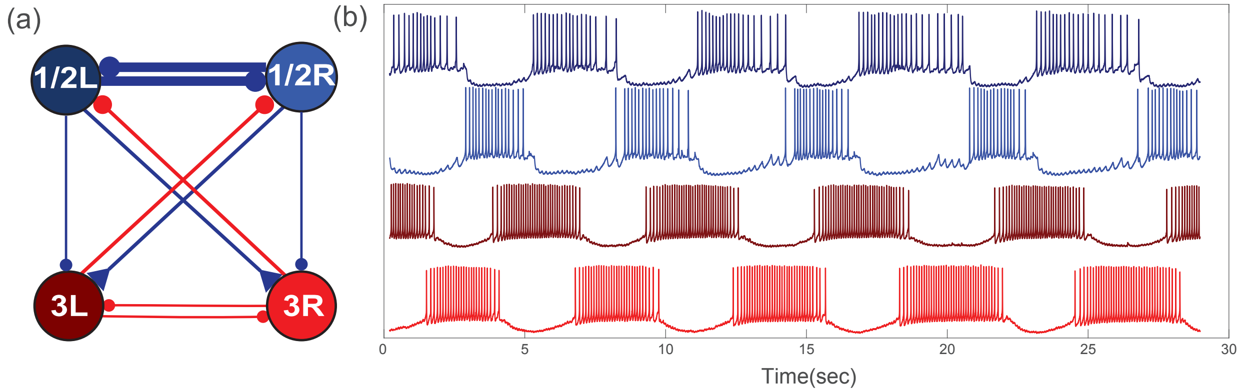

Figure 3.3: (a) Reduced control circuit (b)In-vitro voltage recordings during active swimming. Si2L/R and Si3sL/R burst in anti-phase with a burst duration of 2-4 seconds while Si2s and Si3s burst in a phase locked state. Recordings provided courtesy of A. Sakurai.

Each pair of neurons is connected through HCO mechanism. Unsurprisingly, cells within each pair burst in anti-phase. (i.e., Si2L and Si2R burst in anti-phase, and Si3L and Si3R burst in anti-phase). While each pair is bursting in anti-phase, Si2s and Si3s burst in a phase-locked state in both control and curare cases. In curare case, we observed that there is the delay between burst initiations of contralateral Si2s and Si3s, as well as the tail. All these features are taken into consideration during the modeling process.

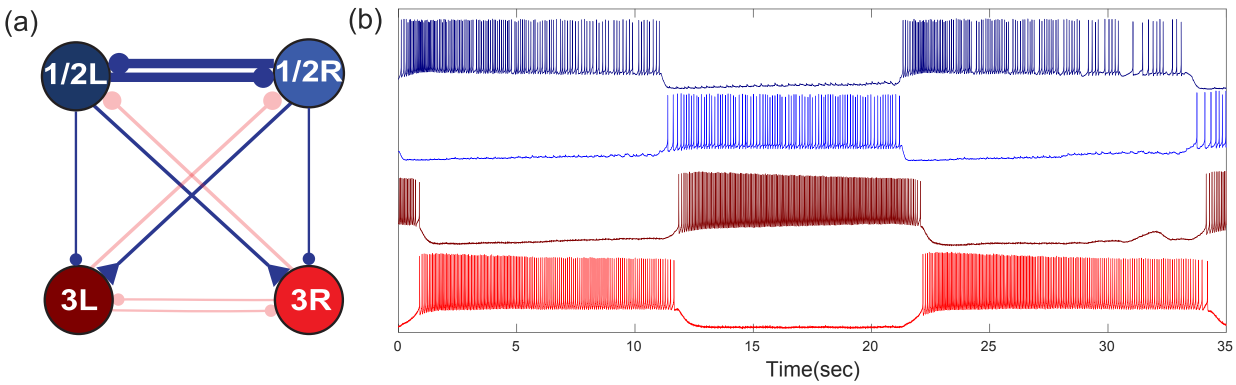

Figure 3.4: (a) Reduced curare circuit (b) Neuro-blocker curare blocks all outgoing connections from Si3s which are reciprocal inhibitory connections between Si3s and the contralateral connections from Si3s onto Si2s. Blockage of these connections yields a significant increase in the burst duration of all cells. The burst duration increases to 12-13 sec while it was 2-4 sec in the control case. The other important feature observed in the curare case is the delay between contralateral Si2s and Si3s. Also, the continuation of Si3s after contralateral Si2s stop bursting is another feature observed in curare case. These two features give us the key points of modeling.Recordings provided courtesy of A. Sakurai.

3.2.2 Mathematical Network

The brain is physically and functionally the most complex part of the body. The connections in a neuronal circuit can be quite complicated which is a challenge for mathematical modeling. To overcome this problem, we used a circuit reduction. The reduced circuit is called the mathematical network to imply that it is different from the original biological circuit and it can be extended to the original version. The reduction procedure was implemented in two steps. The first step of reduction is ruling out Si4s. Si4s are connected to contralateral Si2s via electrical coupling and inhibit the contralateral Si3s. This can be interpreted as an indirect connection from Si2s onto Si3s. Due to the latency in the inhibitory synapse, the burst initiation of Si3s delays. In the biological network, this delay is caused by the existence of Si4s, but in a mathematical point of view, this delay means that the coupling function of the synapse decays slowly. Instead of using an extra cell to create the delay, we used a slowly decaying synapse from Si2s onto ipsi-lateral Si3s. For details, see the methods section.

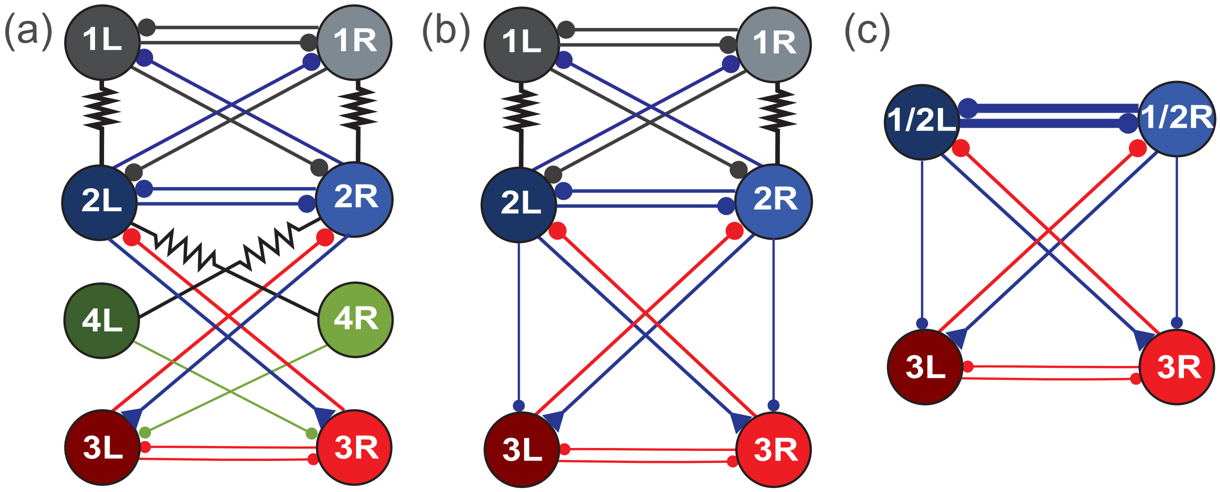

Figure 3.5: (a) Simplified schematic diagram of biological swim CPG which consists of eight swim interneurons. (b) The diagram of CPG after the first step of reduction. (c) The Reduced CPG used in mathematical modeling.

The second step of the reduction process is the merge of the Si1s and Si2s. As mentioned earlier, the CPG consists of four pairs of swim interneurons. One of each pair is located on the left side of the brain, and the other one is to the right of the brain. On both, left and right, sides, the interneurons, ipsilateral Si1s and Si2s, are strongly electrically connected, so they are firing in a highly synchronized manner. Besides the electrical connection, each cell receives inhibition from its contralateral pair and diagonal cell(Fig. 3.5(a)). Merging these two strongly electrically coupled cells into a single cell also requires merge of the inhibitory synapse weights between Si2 around three times representing clustering all three inhibitory connections into one.

Through two-step reduction, we have reduced an eight-cell biological network to a four-cell mathematical network which provides enough simplicity for modeling. Instead of having four different types of neurons, we have two different types of neurons, Si2s and Si3s. Si2s and Si3s have slightly different dynamics in isolation as mentioned earlier.

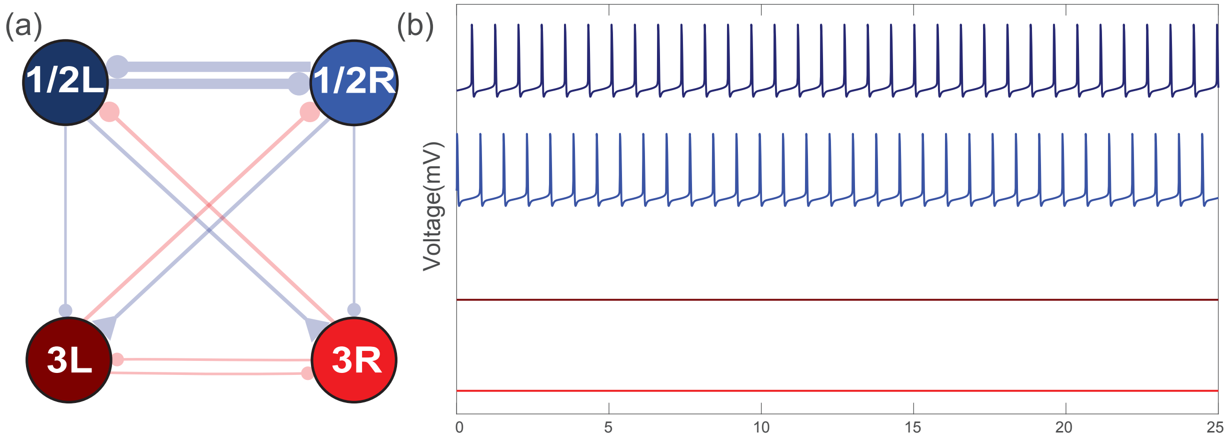

Figure 3.6: Individual cell dynamics are set according to the experimental studies which is presented in Fig 4.1 (d). Experimental results showed Si3s have higher spike frequency than Si2s.

3.3 Model

Biologically plausible circuits constituted by Hodgkin-Huxley (HH) type models of cells coupled by chemical and electrical synapses described by tenable dynamical equations. Based on recent experimental data showing that the individual neurons of the identified swim CPGs never burst endogenously in isolation, we developed a very detailed HH-type model of tonic spiking neurons with multiple time scales. Its key feature is the slow voltage-dependent calcium-based dynamics that provide very good qualitative and quantitative resemblance with dynamics of the biological neurons, and more specifically their responses to perturbations such as external currents synaptic currents. Earlier we developed a pilot, biologically plausible model of the Melibe swim CPG that could realistically reproduce rhythmic outcomes of the real circuit in control, but, unlike the newer model, it failed to meet recent experimental recordings with applications of external perturbations and neuro-blockers such as TTX and curare [68]. Using data assimilation techniques, the new models of neurons and chemical synapses was further fitted to match the dynamics of isolated and networked biological neurons, including their inhibitory and excitatory post-synaptic responses.

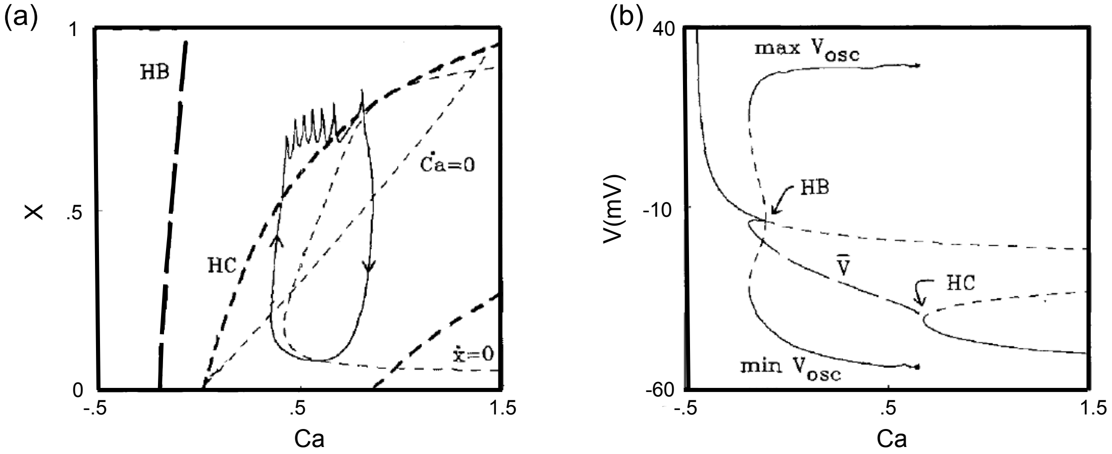

Figure 3.7: (a) Phase plane for slow subsystem ($Ca - x$) plane of the Plant's parabolic bursters model. Curve HC corresponds to degenerate homoclinic orbit (SNIC); periodic solution branch which emerges along HB terminates here. Burst trajectory (solid) reveals that beginning and end of the active phase of spiking corresponds to crossing transition boundary HC between steady state and oscillatory solution branches of equations fast subsystem. Some portions of nullclines have been eliminated. (b) Bifurcation diagram of the system Ca as a parameter. Also shown are max and min values of periodic solutions which arise at HB (subcritical) and terminate in homoclinic orbit HC at saddle-node. Long dashes represent the temporal average of periodic solutions.Figure provided courtesy of Rinzel and Lee [56]

In this chapter, we use a revised version of the earlier model. The model is initially designed for R15 neuron located abdominal ganglion of *Aplysia californica* [46, 47, 48]. R15 neurons are bursters in isolation, and the choice of initial model is inspired by the parabolic burst structure of bursts in some recordings. Parabolic bursters have a low frequency at the beginning and end of the burst, and higher frequency in between. This structure leads us to Plant's parabolic bursters' model [47]. The Hodgkin-Huxley formalism of the previous model to describe the dynamics of the fast inward sodium, I_{Na}, outward potassium I_K, slow TTX-resistant calcium I_{Ca} and an outward calcium-sensitive potassium I_{KCa} currents, the generic ohmic leak I_{leak}, and synaptic I_{syn} currents owing to a pre-synaptic neuron.

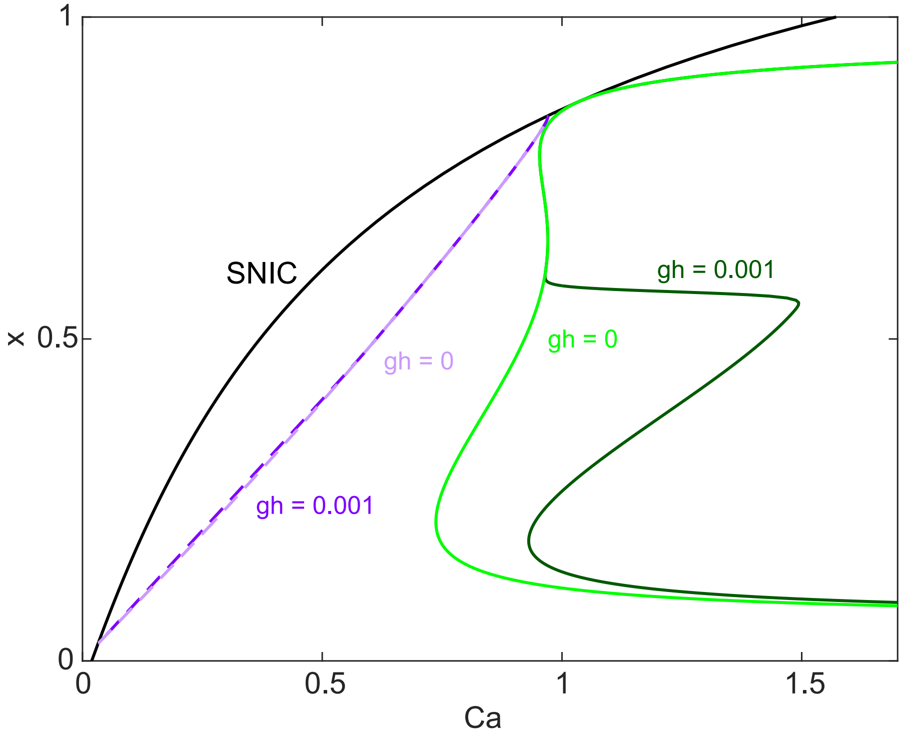

Figure 3.8: Phase portrait of the slow subsystem (Ca-x) with and without h-current. Solid and dashed purple lines represent Ca-nullcline without and with h-current. Dark and light green curves represent x-nullcline without and with h-current where both bifurcation variables are zero ($\Delta_1 = 0$ *and* $\Delta_2 = 0$*). The curve SNIC corresponds to the saddle-node on invariant circle bifurcation.*

In addition to all these existing currents, we added an h-current, I_h, to the system to avoid the deep sags between the bursts. I_h is a hyperpolarization activated depolarizing current [69]. In other words, hyperpolarization of the cell beyond approximately $-50mV$ to $-70mV$, activates h-current and activation of h-current slowly depolarizes the cell towards equilibrium state[69]. This way the deep hyperpolarization in between the bursts are prevented. Fig. 3.8 presents effect of h-current on the phase portrait of slow subsystem. H-current does not have a significant effect on Ca dynamics while it is possible to observe the effect of it on x dynamics. The dark green line in Fig. 3.8 shows where the h-current is activated and the characteristics, h-current added to the system. The burs generation occurs through a SNIC bifurcation similar to the original system. (fig. 3.9) The full details of the currents employed in the model are given in the Appendix B and the fast subsystem is given below:

$$C_m\dot{V} = -I_{Na} - I_K - I_{Ca} - I_{KCa} - I_{leak} - I_h - I_{syn}, \tag{3.1}$$

$$(I_{Na} = g_{Na}m_{\infty}^3(V)h(V - V_{Na}), \quad I_K = g_K n^4(V - V_K), \tag{3.2}$$

$$I_{Ca} = g_{Ca}x(V - V_{Ca}), \quad I_{KCa} = g_{KCa}\frac{[Ca]_i}{0.5 + [Ca]_i}(V - V_K), \tag{3.3}$$

$$I_{leak} = g_L(V - V_L), \quad I_h = g_h(1/(1 + e^{-(V-63)/7.8}))^3 y(V - V_h), \tag{3.4}$$

$$\dot{n} = \frac{n_{\infty}(V) - n}{\tau_n(V)}, \quad \dot{h} = \frac{h_{\infty}(V) - h}{\tau_h(V)}), \tag{3.5}$$

$$\dot{y} = 0.5((1/(1 + e^{10(V-50)} - y)/(7.1 + 10.4/(1 + e^{(V+68)/2.2})). \tag{3.6}$$

Unlike the $R15$ neurons, swim interneurons of Melibe are non-bursters in isolation. Experimental studies show that the cells are tonic spikers or hyperpolarized quiescent cells in isolation. To achieve this property, we used two bifurcation parameters Δ_1 and Δ_2. It is known that reversal potential of calcium ranges between 80-140. These differences led us to add a biologically plausible bifurcation parameter(Δ_1) to the mathematical model (Eq. 3.7). We used this flexibility to change the intrinsic dynamics of the model. In other words, this makes Δ_1 a natural bifurcation parameter. The second bifurcation parameter Δ_2 is to modify the dynamics of the slow variable x. First, we eliminated the bursting state in the model. In other words, we eliminated the hysteresis in the model. We used the slow subsystem to change the dynamics of the system. For $\Delta_2 = -2$, the system has two stable fixed points corresponding to tonic spiking and hyperpolarized quiescent states, and this eliminates the hysteresis or burst generation in isolation in the system.

$$\dot{Ca} = \rho \left[K_c x (V_{Ca} - V + \Delta_1) - [Ca]_i \right], \tag{3.7}$$

$$\dot{x} = ((1/(e^{0.15(-V-50+\Delta_2)} + 1)) - x)/\tau_x, \tag{3.8}$$

Our first assumption is that HCO in between Si2s and Si3s follow different mechanisms, and set the initial dynamics of Si2s as tonic spikers and Si3s as hyperpolarized quiescent cells. Variation of the bifurcation parameter Δ_1 can be interpreted as variation the calcium reversal potential. Revised model can only generate tonic spikers or hyperpolarized quiescent cells same as in the biological network. Since we assume that Si2s and Si3s follow different HCO mechanisms, we set Si2s as tonic spiking cells and Si3s as hyperpolarized quiescent cells. The border of two states is found where $V_{Ca} = 100$ ($\Delta_1 = -40$). The cells are tonic spikers where the V_{Ca} is lower than the border value and hyperpolarized quiescence for higher values. As the value of V_{Ca} gets close to the transition border due to the slow down in the system, the frequency of spiking decreases. In order to imply the differences between Si2s and Si3s, their bifurcation parameters are set according to their intrinsic dynamics such as $\Delta_1 = -44$ ($V_{Ca} = 96$) for Si2s as $\Delta_1 = -36$ ($V_{Ca} = 104$) for Si3s.

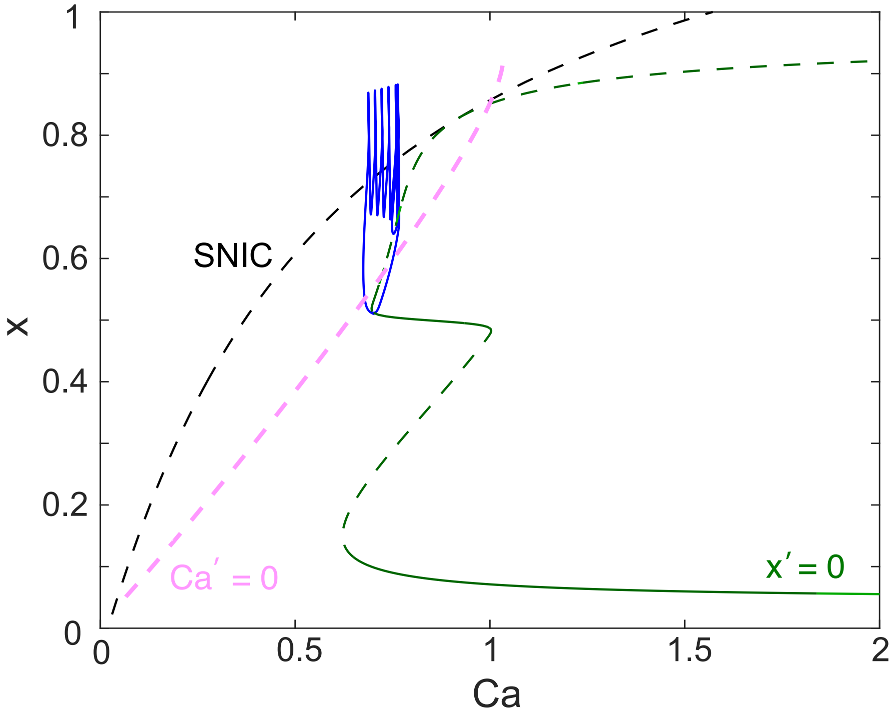

Figure 3.9: Phase portrait of slow subsystem (Ca-x) h-current where both bifurcation parameters are zero ($\Delta_1 = 0$ and $\Delta_2 = 0$). Similar to the previous version of the mathematical model the burst generation occurs through a saddle node on invariant circle (SNIC) bifurcation.

Next, we set endogenous dynamics of each cell, we start putting together the network. In the earlier study, we have used fast threshold modulations(FTMs) for synapses [70]. FTMs are fast synapses and they are modeled as a Boltzmann equation which means that the synapse is either on or off. This type of synapse modeling is an efficient method for fast synapses but it is not a good method for slow synapses that is why instead of FTMs, we use alpha and dynamic synapses which are biologically more plausible. The alpha coupling functions (S) and dynamic coupling function (M) are given by the Eq.3.11. The synaptic current is defined as

$$I_{syn}^{alpha} = g_{syn} S (V_{post} - V_{rev}), \quad I_{syn}^{dyn} = g_{syn} SM (V_{post} - V_{rev}) \tag{3.9}$$

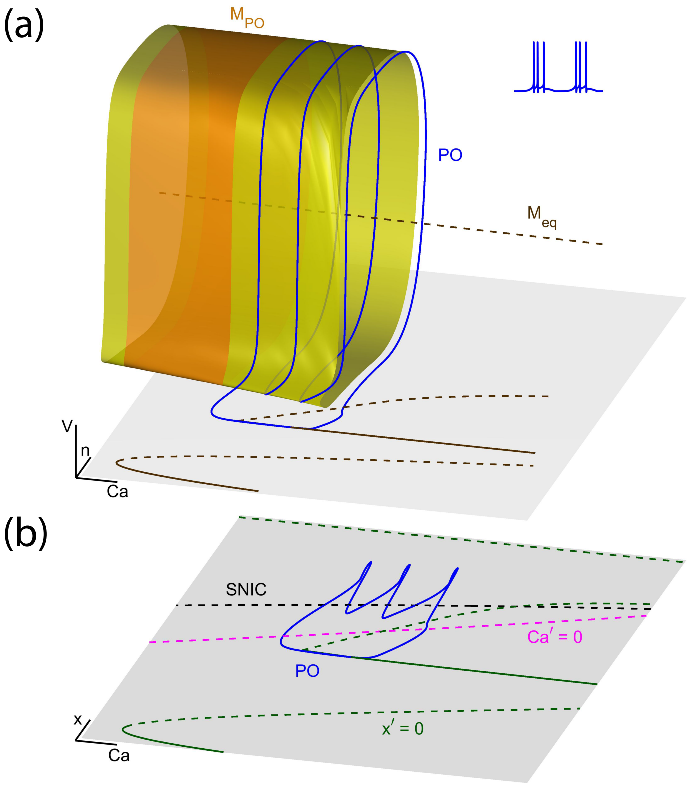

Figure 3.10: 5D phase plane representation of the full system. (a) Bursting (blue curve) orbit rises through a sub-critical Andronov-Hopf (AH) bifurcation in the fast subsystem. Tonic spiking manifold M_{PO} *is represented by the yellow cylinder. (b) Phase plane for the slow subsystem. Blue orbit is the projection of the bursting orbit onto the (x; Ca) where bifurcation parameters* $\Delta_1 = 0$ *and* $\Delta_2 = 0$ *.*

where

$$\dot{S} = \frac{\alpha(1-S)}{1+e^{-k(V-V_{th})}} - \beta S, \tag{3.10}$$

$$\dot{M} = (1/(1+e^{-(V+40)}) - M)/\tau_M \tag{3.11}$$

where g_{syn} is the maximal conductance, V_{rev} is the reversal potential since the network

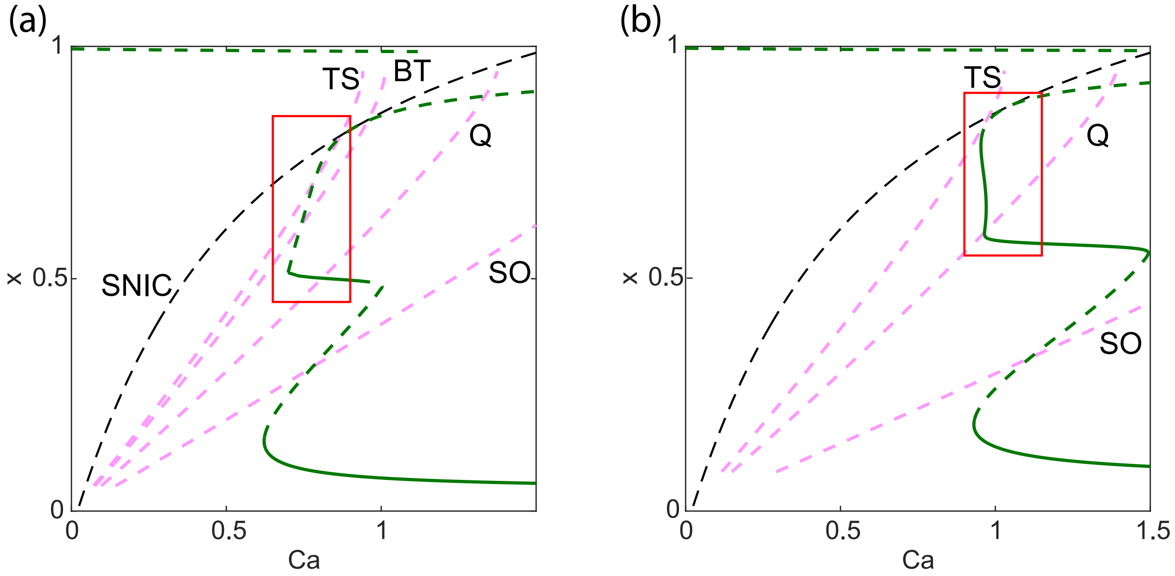

Figure 3.11: Termination of the bursting state. (a)Phase plane of the slow subsystem where $\Delta_1 = -45, -30, 50, 100$ and $\Delta_2 = 0$. The dashed pink lines represent Ca nullcline for given Δ_1 values. Transition between tonic spiking (TS), bursting (BT), quiescent (Q) states and subthreshold oscillations (SO) is possible by the variation of Δ_1. (b)Phase plane of the slow subsystem where $\Delta_1 = -45, 50, 100$ and $\Delta_2 = -2$. The bifurcation parameter Δ_2 shifts the x nullcline horizontally. Shifting is to the right yields termination of the bursting state.

has both inhibitory and synapses and due to the neurophysiological differences between Si2s and Si3s, their reversal potentials are different. We used the experimental values for the reversal potentials for inhibitory synapses $V_{rev}^{Si2} = -80mV$ and $V_{rev}^{Si3} = -50mV$ and excitatory synapses $V_{rev} = -10mV$. α and β values are the rate of increase and decrease for the coupling variable.

3.4 Assembling CPG

In this section, we discuss the step-by-step procedure for assembling the mathematical network. We put together the Melibe swim CPG with the modified mathematical model for the current wiring diagram (given in Fig. 3.2 (b)) based on the experimentally identified

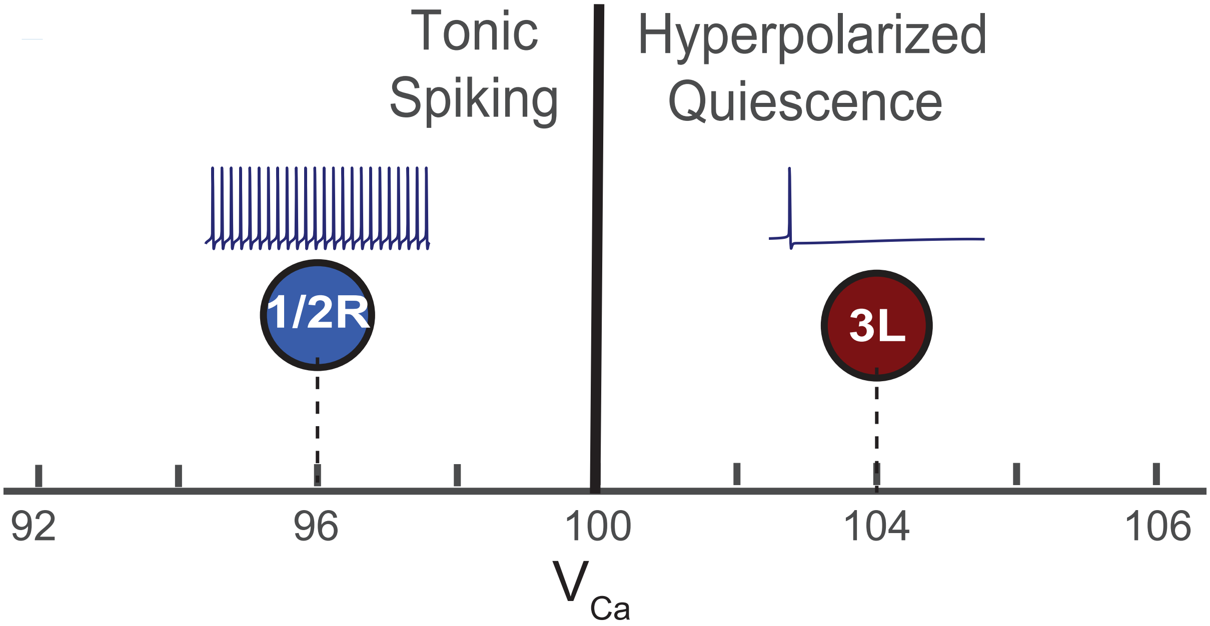

Figure 3.12: The dependence of cell dynamics on calcium reversal potential (V_{Ca}) is shown in the bifurcation diagram. The cells in isolation are in tonic spiking or hyperpolarized quiescent states. In order to qualify the cell properties in our assumptions we set $V_{Ca} = 104$ for Si3s and $V_{Ca} = 96$ for Si2s.

individual cell and synapse dynamics. The fundamental building block of the circuit is HCO. The HCO formed between Si2s comprise the basis of rhythm generation. Our assumption is that HCO between Si2s and Si3s follow different mechanisms in order to generate alternating bursting behavior. There is a strong experimental proof that the Si2 cells are tonic spiking cells in isolation but for dynamics of Si3s are unknown in isolation. It is also known that the cells are network bursters which means that they are non-bursters in isolation. According to what is known about Si3s, we set the intrinsic cell dynamics as hyperpolarized quiescent (Fig./ 3.6), since our assumption is that each pair is generating anti-phase bursting through a different HCO mechanism.

The experimental studies were performed under two different conditions where the animal

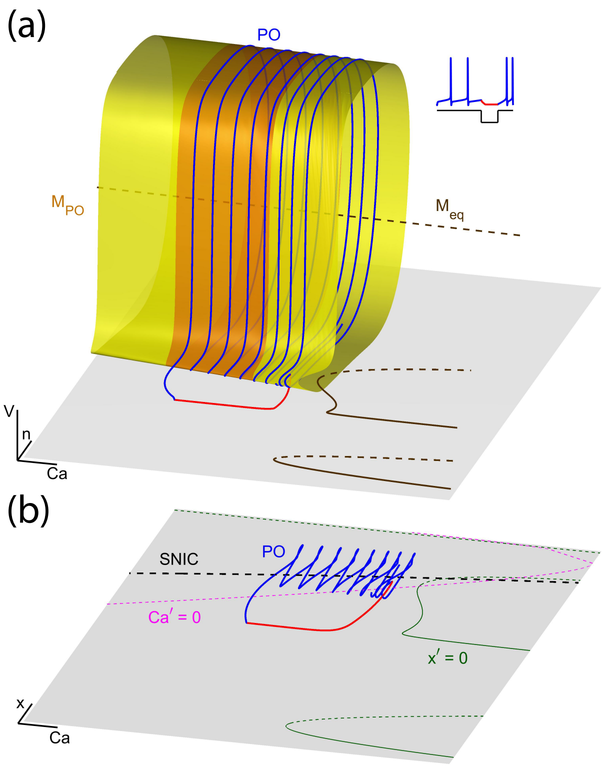

Figure 3.13: 5D phase plane mimicking burst generation through the application of an inhibitory external current to a tonic spiking cell where bifurcation parameters $\Delta_1 = -45$ *and* $\Delta_2 = -2$ *.(a) Application of hyperpolarizing external current (red curve) to a tonic spiking cell yields the transition of the cell towards the quiescent state. The tonic spiking orbit is represented by the blue curve, and the application of the external current is represented by the red section of the orbit. (b) Projection of the burst generation onto the phase plane of the slow subsystem. Blue orbit is the projection of the bursting orbit onto the (x; Ca) plane where red section represents the hyperpolarized applied current.*

exhibits normal swim behavior (control case) and the existence of a neuroblocker which blocks all the outgoing synapses of Si3s (curare case). The properties of both cases are explained in detail in previous chapters, and also brief information is given in the biological network section. To create a more plausible model and calibrate the synapses properly, we started the assembly from the curare case which is a simpler circuit compared to the control circuit. Curare circuit includes half-center oscillators between Si2s, ipsilateral inhibitory synapses and contra-lateral excitatory synapses from Si2s onto Si3s (Fig. 3.4(a)).

Previously, we used FTMs to model synapses in the model. FTMs are a simple and efficient modeling technique for fast synapses but failed to meet the properties of the slow synapses which plays a significant role in rhythm generation in the circuit. The previous model with FTMs was able to capture the characteristics of control case but failed to meet the characteristics of curare case. We replaced FTMs with alpha synapses, and for slower synapses such as contralateral excitation, we used dynamic synapses which are biologically more plausible synapse models.

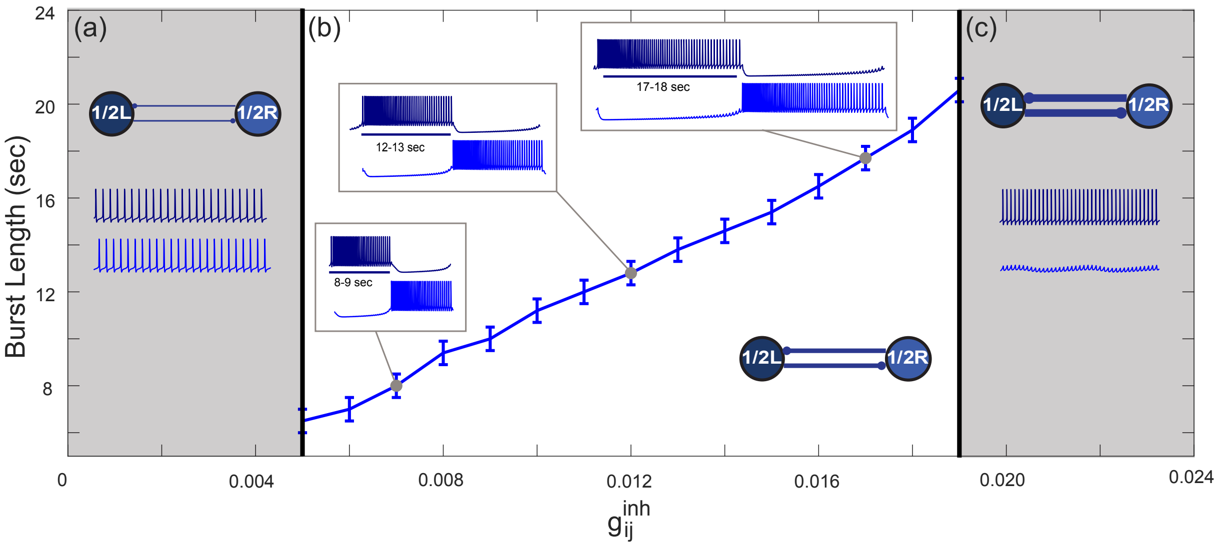

Figure 3.14: Burst duration of Si2s in curare case depends on reciprocal inhibitory connection strength. (a) For weaker values of inhibitory connection strength ($g_{ij}^{inh} < 0.005$), cells maintain tonic spiking (b) Increasing the connection strength ($0.005 \leq g_{ij}^{inh} \leq 0.019$) causes an increase in the burst duration. (c) Increasing the connection strength further ($g_{ij}^{inh} > 0.019$) results one cell to maintain tonic spiking while the other cell goes quiescent. The desired burst length for curare case, 12-13 sec, is obtained for $g_{ij} = 0.012$.

We start assembling the circuit from curare case since it has a less complicated wiring diagram. Since Si3s are quiescent cells, the network characteristics will be determined by the dynamics of Si2s. Si3s will follow the Si2 dynamics through the contralateral excitatory coupling. Experimental studies showed that the inhibitory synapses between Si2s are fast synapses, so the α and β values of the coupling variable is chosen accordingly where $\alpha = 0.05$ and $\beta = 0.005$. The most significant feature of the curare network is the burst duration of the network. The burst duration in curare network lasts around 12-13 seconds. The specific burst duration of the network is controlled by the burst duration of Si2s. One of the features of the mathematical model is the structure of recovery period which is controlled by the slow subsystem. The longer recovery period of post-cell means longer burst duration of pre-cell. In other words, stronger synaptic strength causes longer recovery time and longer recovery time causes longer burst duration. The dependence of burst duration on synaptic strength is summarized in Fig. 3.14. For weaker values of inhibition, the cells keep tonic spiking ($0 < g_{ij}^{inh} < 0.005$). As the strength of inhibition increases the cells start anti-phase bursting and the burst duration lasts longer with stronger inhibition values ($0.005 \leq g_{ij}^{inh} \leq 0.020$). As the coupling strength keeps getting stronger, eventually one of the cells shuts down the other one ($g_{ij}^{inh} > 0.020$). In order to meet the experimental results, we set the coupling strength at a level which gives desired 12-13 sec burst length ($g_{ij}^{inh} = 0.012$).

Another typical characteristic of the curare network is the delay between the burst initiation and the continuation of spiking activity after Si2 goes to quiescent state what we refer as the tail of the contralateral Si2s and Si3s (i.e., Si2L-Si3R and Si2R-Si3L). The delay and tail are controlled by the interactions between the ipsilateral inhibition and the contralateral excitation. Quiescent Si3s follow voltage activities of contralateral Si2s, so contralateral

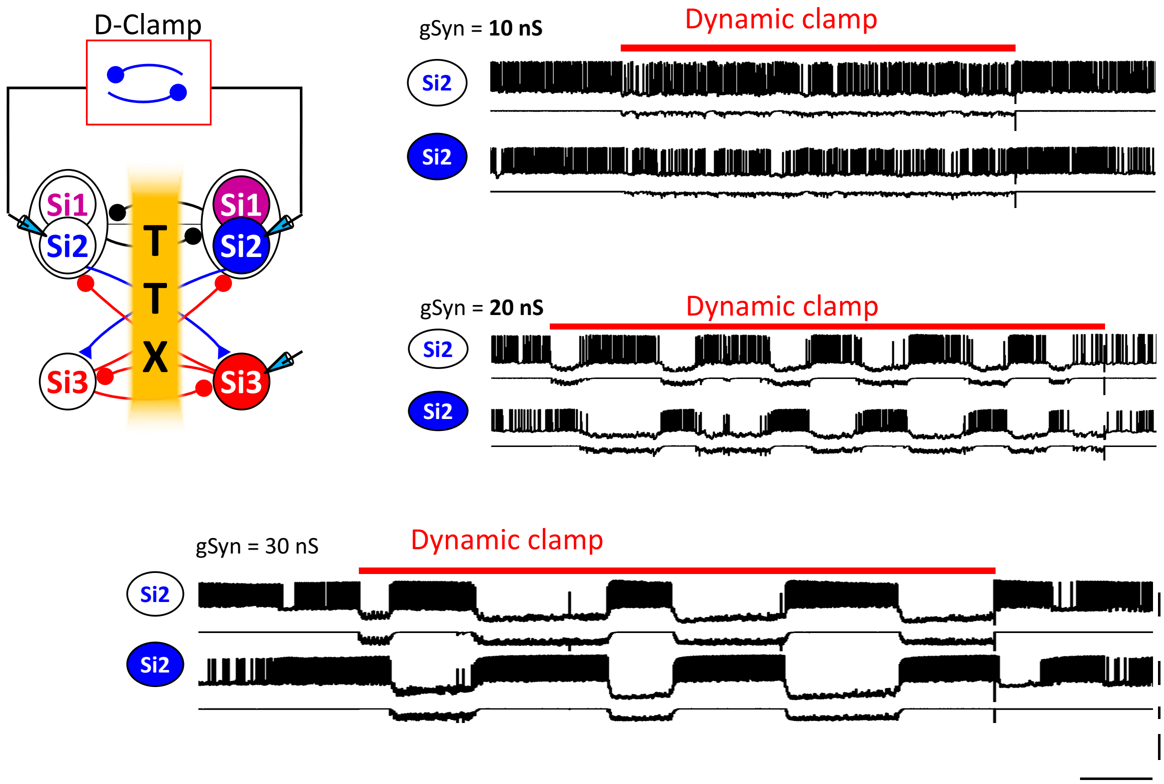

Figure 3.15: The inhibitory connections between Si2s are recovered by dynamic-clamp technique during application of TTX. As the connection strength increases the burst duration increases as well. This experimental result is verified with the simulation results(See Fig. 3.14). Courtesy of A. Sakurai.

excitatory synapse dynamics play an important role in the generation this specific feature. Excitatory synapses build slowly so the ipsilateral inhibition can overrule excitation and delay the burst initiation. The tail also depends on the dynamics of the excitatory synapse. The slow decay of excitatory synapse overrules the ipsilateral inhibition during its building up period, so Si3s keep bursting until coupling variable of the excitatory synapse goes to zero.

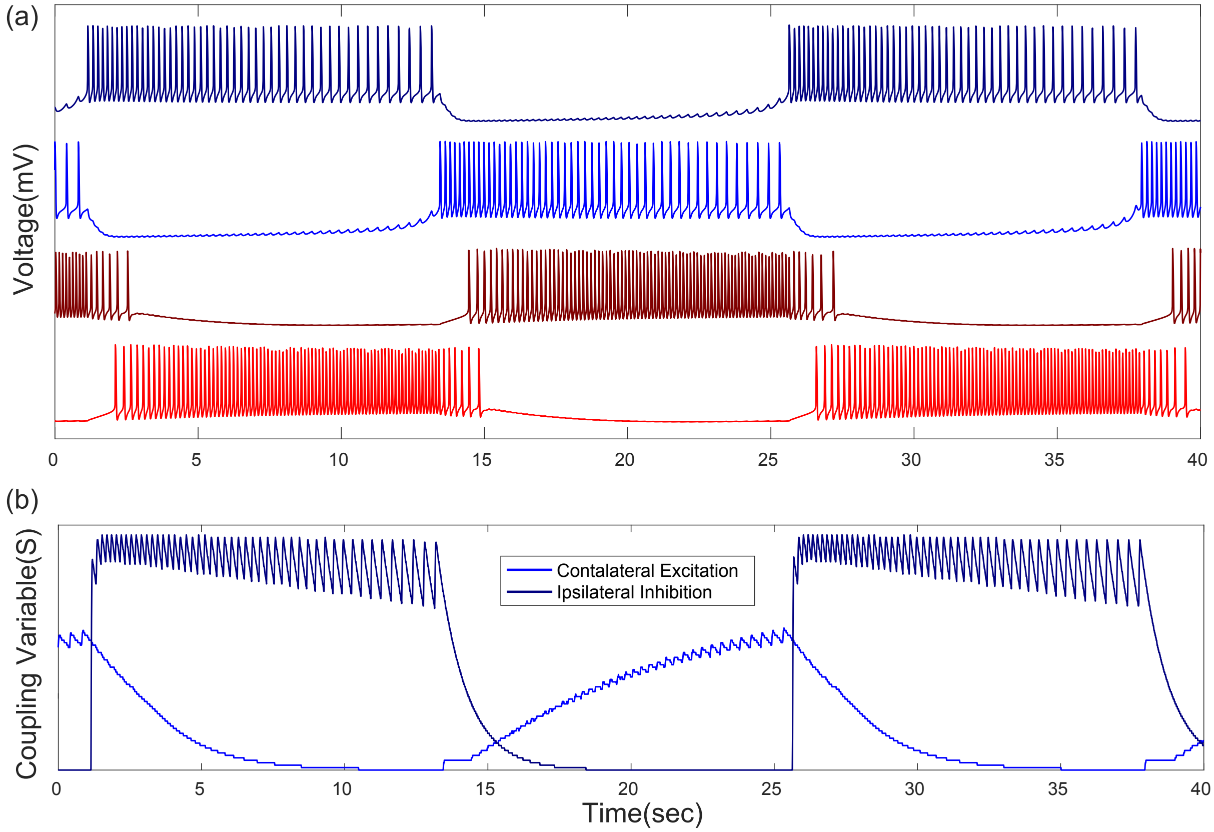

Figure 3.16: (a) Simulation results for curare network Si2L/R and Si3sL/R burst in anti-phase with a burst duration of 11-12 seconds with characteristics of what we call delay and tail. (b) Dynamics of coupling functions for ipsilateral inhibition from Si2s onto Si3s (dark blue) and contralateral excitation from Si2s onto contralateral Si3s (blue).

Next, we continue with restoring the blocked connections to assemble the control network. There is a significant difference in curare and control networks in curare and control cases. The burst duration is between 2-4 seconds in control network while it is 12-13 seconds in curare network. We have examined the dependence of burst duration on synaptic strength in Si2s, and it is observed that 2-4 sec burst duration generation is not possible to obtain between Si2s. This burst duration can only be generated with the reactivation of contralateral inhibition from Si3s onto Si2s. As the coupling strength of the synapse is increased the

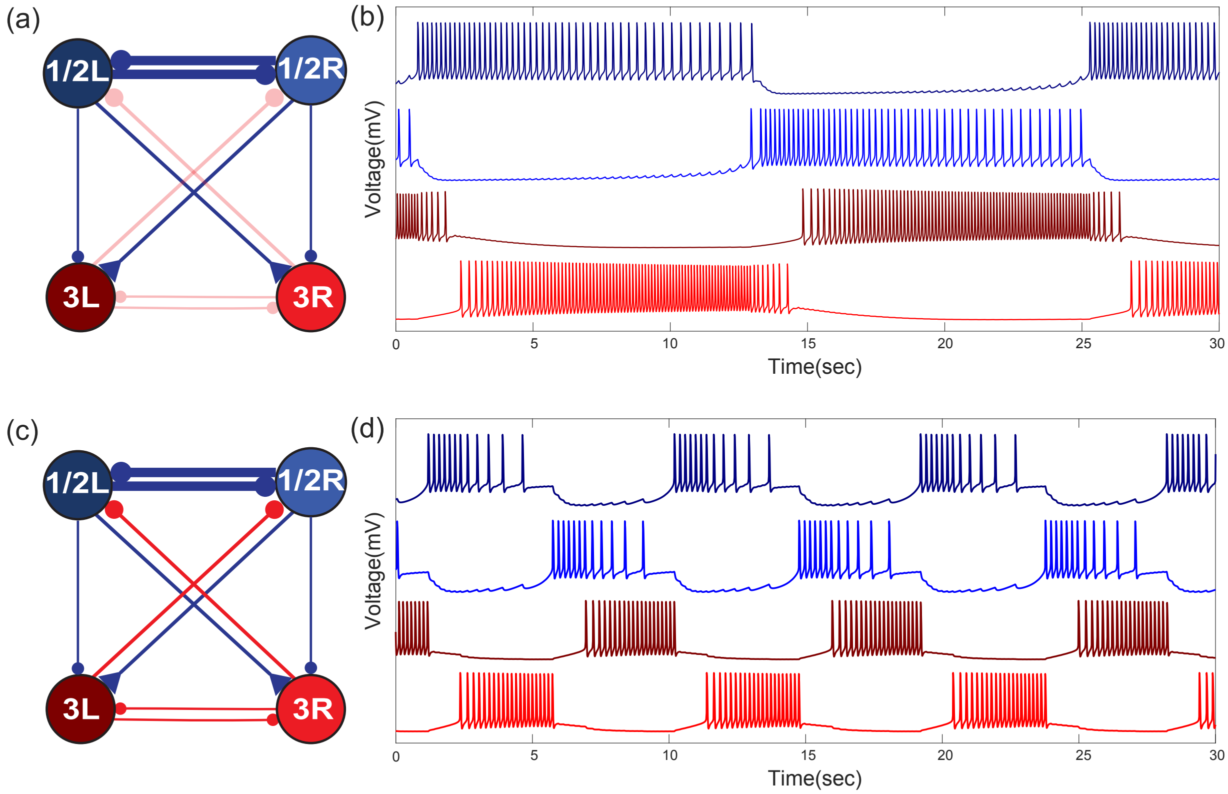

Figure 3.17: (a) Reduced curare circuit (b)Simulation results for curare network Si2L/R and Si3sL/R burst in anti-phase with a burst duration of 11-12 seconds with characteristics of what we call delay and tail. (c) Reduced control circuit (d) Simulation results for control network. Si2L/R and Si3sL/R burst in anti-phase with a burst duration of 2-4 seconds while Si2s and Si3s burst in a phase locked state.

burst frequency of the network increases. Dependence of the network burst duration on the strength of contralateral inhibition is examined in detail in the next chapter. The network can generate the desired burst length for $g_{inh} = 0.004$.

The last characteristic of the control network is the delay between contra-lateral Si2s and Si3s. In curare network, this delay is controlled by the interaction between contralateral excitation and ipsilateral inhibition. Restoring the inhibitory synapses between Si3s adds robustness to the network. It is also observed that as the strength of inhibition increases the delay is increasing as well. Fig. 3.17 presents the voltage traces generated by the mathematical model for both curare network and control network.

3.5 Summary

In this chapter, we have used a revised version of the previous model and discussed the workflow of the building network bursting of the Melibe swim CPG which is composed of tonic spiking and quiescent cells. The initial model, Plant's parabolic bursters model, was developed for R15 cells in *Aplysia* which are intrinsic bursting cells. The experimental studies showed that the Melibe cells are either tonic-spiking or hyperpolarized quiescent cells in isolation, unlike R15 cells. More specifically, it was shown that the SI2s are tonic spiking cells, but there was no experimental data showing the intrinsic dynamics of Si3s. Our first assumption was that the Si2 and Si3 pairs follow different mechanism for HCO generation. Accordingly, we have assumed that Si2s are tonic spiking cells and Si3s are hyperpolarized quiescent cells. First modification we have made in the mathematical model is to eliminate the bursting state. The bursting state of the model is eliminated by using bifurcation theory. Previously, we have examined the model responses to the perturbations and identified the transition boundaries. We have introduced a second bifurcation parameter to the slow subsystem. Variation of the second bifurcation parameter terminated the bursting state so the revised model can only generate tonic spiking or hyperpolarized quiescent cells. First, we have set the intrinsic dynamics of the cells set as tonic spikers for Si2s and hyperpolarized quiescent for Si3s through. We followed a similar path to the previous case for assembling the network. We started by assembling the Si2 HCO, and unlike the previous model, here we have used slow synapse dynamics instead of FTM. Synapses are modeled by alpha and dynamic synapse models. New experimental results have revealed new features of the network. Our goal is to capture all these features of the biological network with the mathematical model. The first feature, we wanted to adapt to the model was the burst duration in the curare network which is around 11-13 secs. We have continued assembly of the network with the curare network which has a simpler wiring diagram. We successfully generated the characteristics of the curare network such as the burst duration, delay, and tail. Finally, we have recovered the blocked connections to reach the control network. As a result of slow synapse dynamics, we were able to generate the characteristics of the control case such as 2-4 sec burst duration and the delay between contralateral cells in the network.

As mentioned earlier, the identification process of the Melibe swim CPG is still an ongoing work, and the most recent experimental studies revealed that both Si2s and Si3s are tonic spiking cell in isolation. These new findings require recalibration of the mathematical model. In the next chapter, we will present the process of assembling the network for tonic spiking cells and slow synapses. We will also verify the mathematical model by performing the experimental studies with the mathematical model and compare the experimental results with the simulation results.

CHAPTER 4

DETAILED MODELING AND MODEL VERIFICATION

4.1 Introduction

Melibe leonina swims with a rhythmic behavior of flexing its body laterally, left and right, and this behavior is regulated by a small neuronal circuit. These type of small neuronal circuits, central pattern generators(CPGs), can generate rhythmic activity without a sensory feedback and are believed to control animal behavior like heartbeat, walking, flying, breathing and swimming [1, 2, 3, 71, 4, 5]. CPGs are the building blocks of the central nervous system. Thus, understanding CPGs is the first step of understanding complex neuronal structures in the central nervous system. The joint work of computational and neuro-physiological researchers is focused on enlightening the underlying rhythm generation mechanism of these type of neuronal circuits. Mathematical models are effective tools for this purpose, but despite broad studies and existence of a variety of mathematical models, working principles of these mechanisms remain mysterious.

We would like to develop a highly detailed mathematical model for the swim CPG of *Melibe Leonina* and make it a biologically as plausible as possible. In previous chapters, the model development process is explained. In the second chapter, the initial model, Plant's parabolic bursters model, is able to produce the rhythm generated during the swim but failed to meet recent experimental findings such as the delay between burst initiation of contralateral Si2s and Si3s in curare case or the continuation of spiking (tail) after Si2s goes to the quiescent state. Also, FTMs are suitable for modeling fast synapses, but the

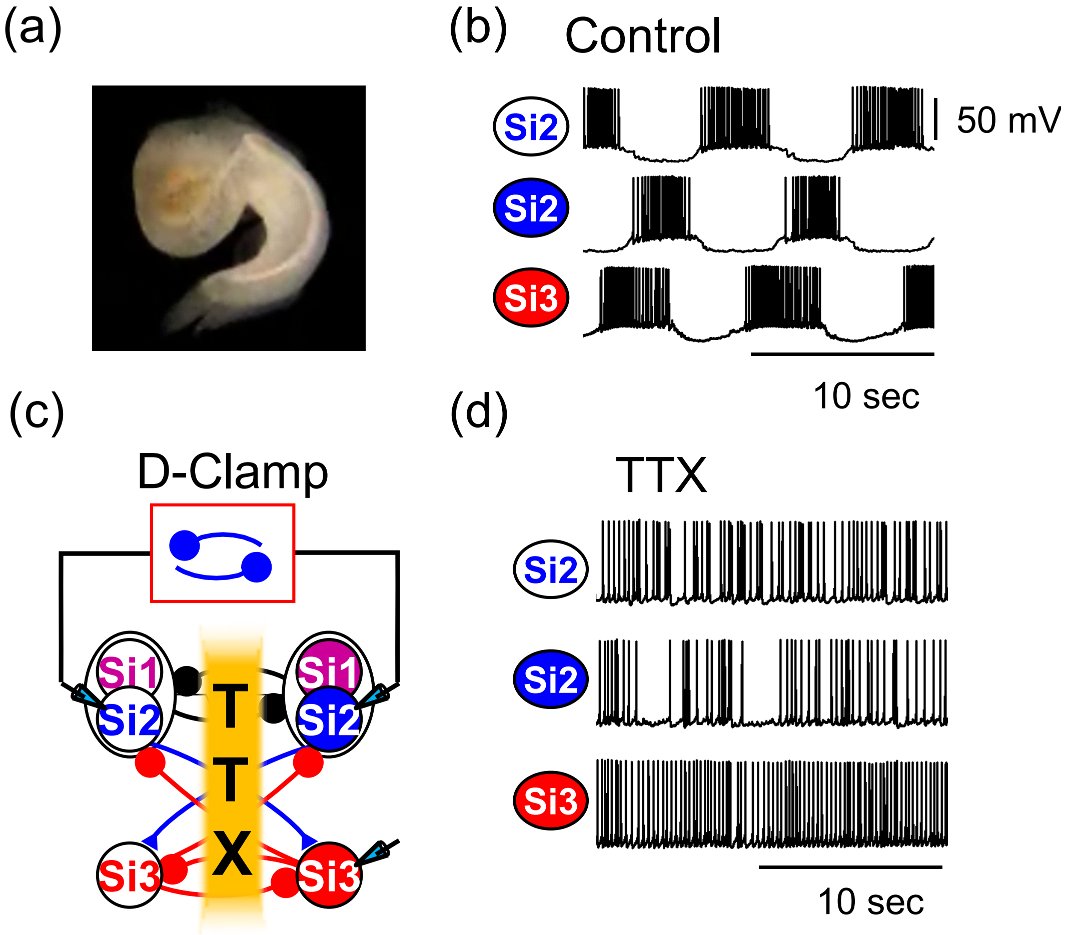

Figure 4.1: (a)Melibe leonina body flexing during the swim activity. (b) Voltage activity during the swim. (c) Effect of TTX on the biological network. (d) Voltage traces with under TTX effect. Recordings provided courtesy of A. Sakurai.

Melibe swim CPG has slow synapses besides fast ones. In the third chapter, we replaced FTMs with alpha synapses to be able to implement the slow dynamics of the synapses to the model. Detailed information about alpha and dynamics synapses are given in chapter 3. Another detail that we considered in chapter 3, the cells in isolation is either in tonic spiking state or hyperpolarized quiescent state. The experimental studies showed that they are non-bursting cells in isolation and experiments proved that the Si2s are tonic spikers. According to the experimental results, we eliminated bursting state in the mathematical model. Unlike Si2s, there was not a particular information about the behavior of Si3s in isolation, but the findings were enough to say that HCO mechanisms between Si2s and Si3s are different. That is why we have considered Si2s as tonic spiking cells and Si3s as hyperpolarized quiescent cells in isolation. The second model was more successful to capture the characteristics of the network, but the more recent experimental results showed that all cells are tonic spiking cells in isolation(Fig. 4.1).

In this final chapter for modeling Melibe swim CPG, we considered that all cells are tonic spiking cells. Experimental studies also revealed that spike frequency Si3s is higher firing rate than Si2s. The difference in firing frequencies plays a significant role in synapses since the coupling function has non-linear dependence on the spike frequency of pre-synaptic cell. The characteristic of coupling function is the key feature of slow and fast synapses. Details of modeling process are given in the following sections.

4.2 Model

Tetrodotoxin (TTX) is a neuro-toxin that blocks the sodium channels. It inhibits the firing of action potentials in neurons by blocking the passage of sodium ions into the neuron. In the Melibe swim CPG, TTX which blocks potential action transmission along the axons that connect the two halves of the brain, effectively disconnecting those synapses. Applying TTX to the network gave us the opportunity to examine the intrinsic cell dynamics (Fig. 4.1). Previously, we assumed that Si2 and Si3 pair follow different HCO mechanisms and their intrinsic dynamic are different. According to the recent experimental results, this assumption is not valid, and the intrinsic cell dynamics are quite similar to each other. TTX experiment showed that all the cells in the mathematical network are tonic spikers but the spike frequency of Si2s and Si3s are significantly different than each other. Si3s due to their smaller physical size have higher frequency compared to Si2s.

We revised the mathematical model according to the new findings. We used the same model as in the previous chapter and added more details for cell and synapse dynamics. The Hodgkin-Huxley formalism for the voltage value and the currents are given below in closed form the details are given in the previous chapter and appendix.

$$C_m\dot{V} = -I_{Na} - I_K - I_{Ca} - I_{KCa} - I_h - I_{leak} - I_{syn} \tag{4.1}$$

As mentioned earlier, there are two different bifurcation parameters for each slow variable in the system: Δ_1 and Δ_2. Earlier we have discussed that for $\Delta_2 = -2$ there are only two states exist: tonic spiking and hyperpolarized quiescent. It is known that reversal potential of calcium ranges between 80-140. We used this flexibility to change the intrinsic dynamics of the model and set the initial dynamics of the cells as tonic spikers as in the biological CPG. In other words,this makes Δ_1 a natural bifurcation parameter.

$$\dot{Ca} = \rho\left[K_c x(V_{Ca} - V + \Delta_1) - [Ca]_i\right], \tag{4.2}$$

$$\dot{x} = ((1/(e^{0.15*(-V-50+\Delta_2)} + 1)) - x)/\tau_x, \tag{4.3}$$

Variation of the bifurcation parameter Δ_1 can be interpreted as variation the calcium reversal potential. The border of two states is found where $V_{Ca} = 100$ ($\Delta_1 = -40$). The cells are tonic spikers where the V_{Ca} is lower than the border value and hyperpolarized quiescence for higher values. As the the value of V_{Ca} gets close to the transition border due to the slow down in the system, the frequency of spiking decreases. In order to imply the frequency differences between Si2s and Si3s, their bifurcation parameters are set according to their spiking frequencies such as $\Delta_1 = -44$ ($V_{Ca} = 96$) for Si2s as $\Delta_1 = -54$ ($V_{Ca} = 86$) for Si3s.

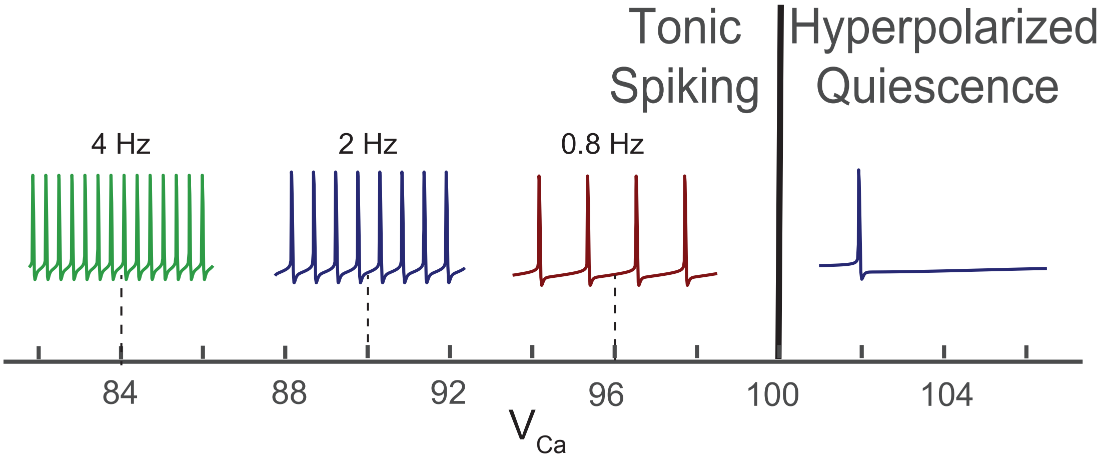

Figure 4.2: The dependence of firing frequency on calcium reversal potential (V_{Ca}) is shown in the bifurcation diagram. The cells in isolation are in tonic spiking or hyperpolarized quiescent states. As the cells, get closer to the boundary line ($V_{Ca} = 100$), spiking frequency decreases.

After setting endogenous dynamics of each cell, we start putting together the network. In the earlier study, we have used fast threshold modulations(FTMs) for synapses [70]. FTMs are fast synapses and they are modeled as a Botlzmann equation which means that the synapse is either on or off. This type of synapses are not realistic for a biological network that is why instead of FTMs we use alpha and dynamic synapses which are biologically more plausible. The alpha coupling function (S) and dynamic coupling functions are given by the

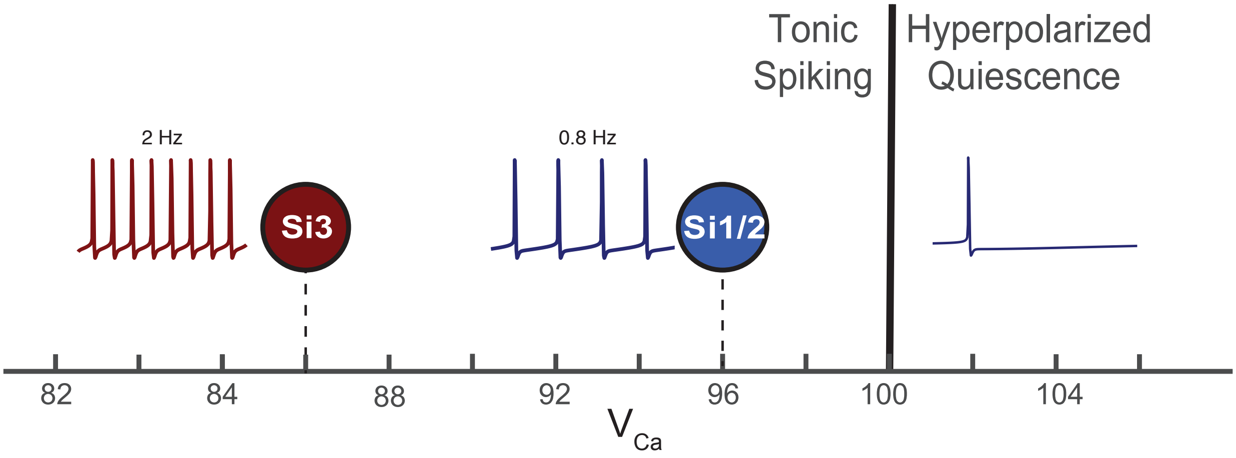

Figure 4.3: The dependence of firing frequency on calcium reversal potential (V_{Ca}) is shown in the bifurcation diagram. The cells in isolation are in tonic spiking or hyperpolarized quiescent states. As the cells, get closer to the boundary line ($V_{Ca} = 100$), spiking frequency decreases. In order to qualify the cell properties through TTX experiment, V_{Ca} values for each cell type is chosen accordingly. ($V_{Ca} = 86$ for Si3s and $V_{Ca} = 96$ for Si2s.

Eq.4.6. The synaptic current is defined as

$$I_{syn}^{alpha} = g_{syn}S(V_{post} - V_{rev}), \quad I_{syn}^{dyn} = g_{syn}SM(V_{post} - V_{rev}) \tag{4.4}$$

where

$$\dot{S} = \frac{\alpha(1-S)}{1+e^{-k(V-V_{th})}} - \beta S, \tag{4.5}$$

$$\dot{M} = (1/(1+e^{-(V+40)}) - M)/\tau_M \tag{4.6}$$

where g_{syn} is the maximal conductance, V_{rev} is the reversal potential since the network has both inhibitory and synapses and due to the neuropyhsiological differences between Si2s and Si3s, their reversal potentials are different. We used the experimental values for the reversal potentials for inhibitory synapses $V_{rev}^{Si2} = -80mV$ and $V_{rev}^{Si3} = -50mV$ and excitatory synapses $V_{rev} = -10mV$. α and β values are the rate of increase and decrease for the coupling variable.

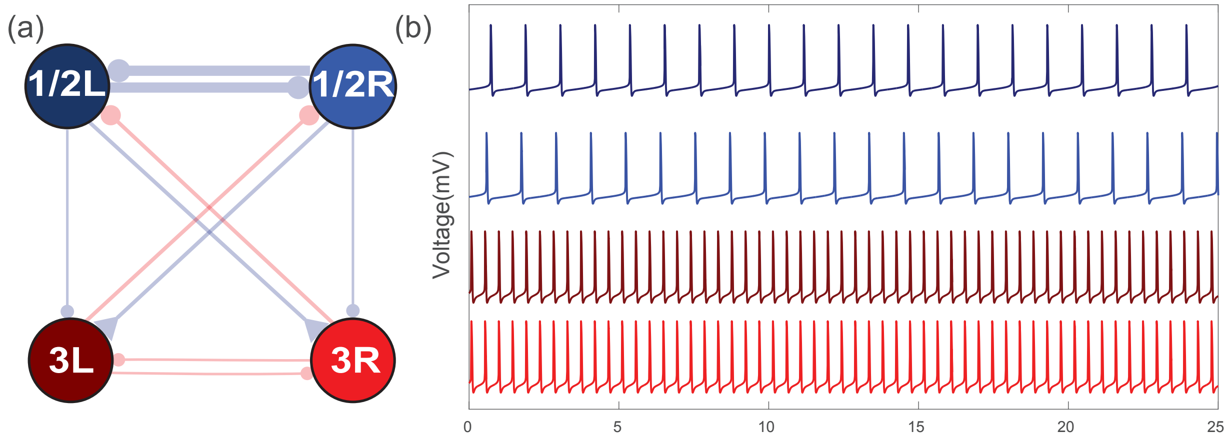

Figure 4.4: Individual cell dynamics are set according to the experimental studies which is presented in Fig 4.1 (d). Experimental results showed Si3s have higher spike frequency than Si2s.

In the network, some synapses are identified as slow, and some are fast through experimental studies. In the mathematical model, the dynamics of the synapse depends on the frequency of the pre-cell and this case is explained in detail in the next section. The dynamics of a synapse also depends on the increase and decrease rate of the coupling function: α and β. Depending on this experimental results, we have defined different coupling functions for each synapse. Coupling functions for each synapse type are given in Table 4.1. In the table, S_{inh}^{Si2} is inhibitory synapses between Si2s, S_{inh}^{Si3} is the inhibitory synapses between Si3s, S_{inh}^{contra} is the inhibitory synapses from Si3s onto contralateral Si2s, S_{inh}^{ipsi} is the inhibitory synapses from Si2s onto ipsi-lateral Si3s and S_{exc}^{contra} is the excitatory synapses from Si2s onto contralateral Si3s.

Synapse Type	α	β
S_{inh}^{Si2}	0.05	0.005
S_{inh}^{Si3}	0.02	0.002
S_{inh}^{contra}	0.02	0.003
S_{inh}^{ipsi}	0.05	0.001
S_{exc}^{contra}	0.05	0.0003

Table 4.1: Increase (α) and decrease (β) rates for each synapse type

4.3 Assembling the Network

In this section, we discuss the step-by-step procedure of assembling the mathematical network similarly to the previous chapter. Experimental studies provided detailed information about the network. During the mathematical model development process details of the biological network are implemented into the mathematical model as much as possible. From the experiments, it is known that each type of cell and each synapse has its specific characteristics. We started with the characteristics of each cell in the network. The experimental studies on Melibe swim CPG reveal a new feature of the network in each experiment. In the previous chapter, our assumption was that Si2s and Si3s generate alternating bursting activity through different HCO mechanisms and that is why we chose different intrinsic dynamics for Si2s and Si3s. The latest studies revealed that both Si2s and Si3s are tonic spiking cells. The differences in endogenous dynamics of Si2s and Si3s are the spike frequency and inhibitory reversal potential. After setting the single cell dynamics, we started putting the network together.

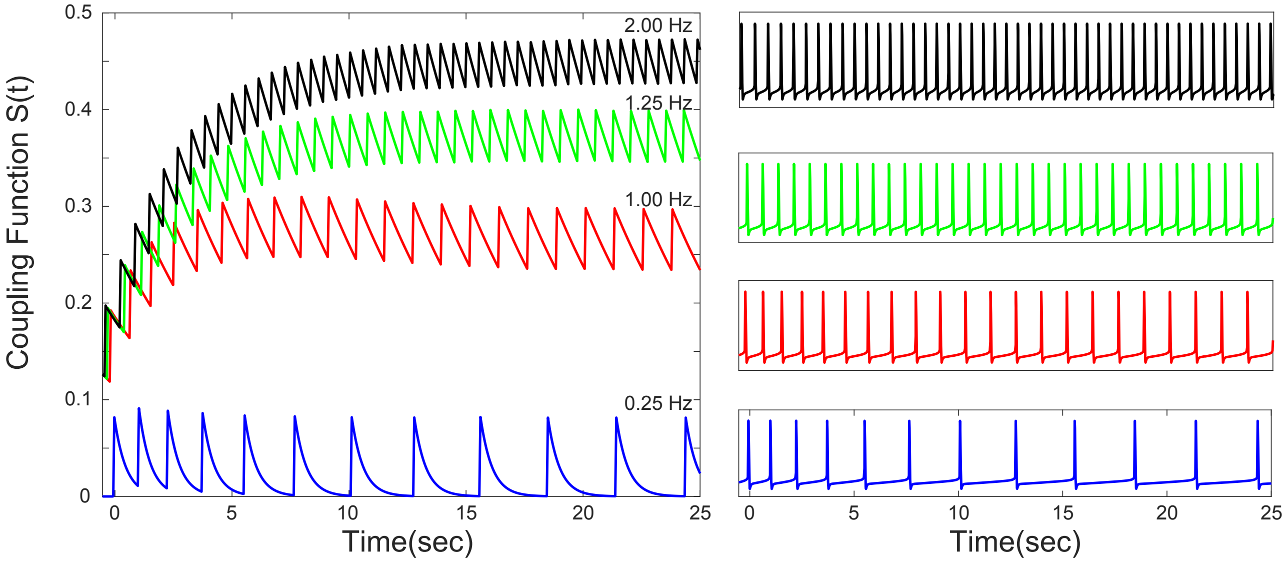

Figure 4.5: Nonlinear dependence of cumulative coupling strength on the high spike-frequency rate in presynaptic neurons is imperative for slow excitatory and inhibitory chemical synapses to regulate neurotransmitter release and to activate synaptic feedback loops for elastically maintaining the CPG temporal characteristics.

In the previous chapter, we explained that the method to model synapses is changed from FTMs to alpha and dynamic synapses which are biologically more plausible modeling methods. Previously, we used the same type of alpha synapses for all inhibitory synapses. In this chapter, we define an individual coupling variable for each inhibitory synapse depending on the dynamics described in experimental studies. The inhibitory synapses between Si2s and the ipsilateral inhibitory synapses from Si2s onto Si3s are faster compared to the contralateral inhibition from Si3s to Si2s and inhibition between Si3s. The α and β values for each synapse type is given in the appendix.

The most important feature of the synapses is the nonlinear dependence of cumulative coupling strength on the high spike-frequency rate in presynaptic neurons. This is imperative for slow excitatory and inhibitory chemical synapses to regulate neurotransmitter release and to activate synaptic feedback loops for elastically maintaining the CPG temporal characteristics. The dependence of synaptic variable on frequency is critical component of the rhythm generation process.

We start assembling the network again similar to the previous chapter from the curare network due to the simple wiring diagram of the network. Curare network is composed of the HCO of Si2s, contralateral excitation and ipsilateral inhibition from Si2s onto Si3s. Similar to the previous case, the burst duration of the network is controlled by the Si2 pair. We set the inhibitory coupling strength between Si2s to a value, so the burst duration is around 12-13 seconds. Remember that in the previous chapter, Si3s were set to a state where they are in hyperpolarized quiescent state in isolation. Here, they are considered as tonic spiking cells in isolation as Si2 cells. Since Si3s are tonic spiking cells, the ipsilateral inhibitory synapses play a very important role in transition of Si3s to bursting state. While Si2s are in active phase, the ipsilateral inhibition gets activated and shuts down the ipsilateral Si3s. At the same time, the contralateral excitation also gets activated and pulls the voltage value towards the bursting threshold.

The second characteristic of the curare network is the delay and tail between the contralateral Si2s and Si3s. This feature is a result of the interactions between ipsilateral inhibition and contralateral excitation. The details are given in the previous chapter, so we will not go over the details in here. The assembled curare network and voltage traces of the simulations are given in Fig. 4.6.

Next, we will restore the synapses blocked by curare to assemble the control network. We

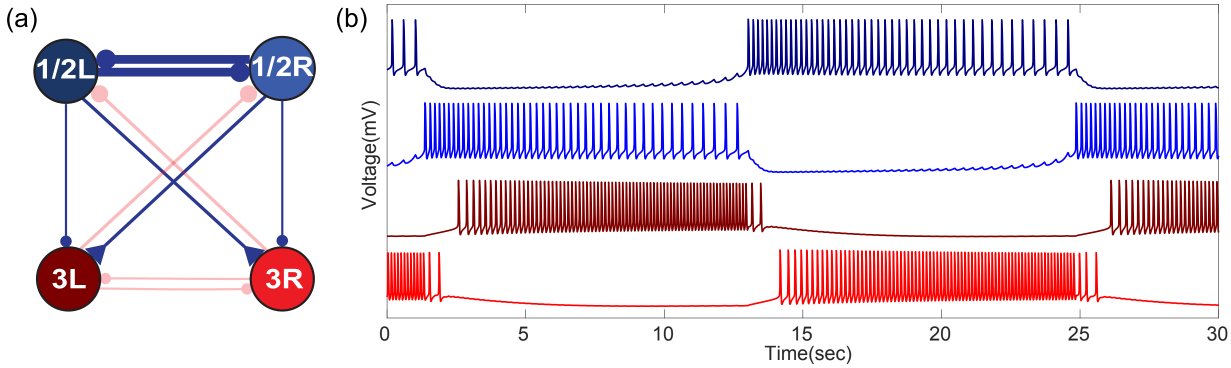

Figure 4.6: Assembling curare network for mathematical model. Burst duration of Si2s is fixed to 12-13 sec through the strength of reciprocal inhibitory connections between them. The ipsilateral inhibition from Si2s onto Si3s pushed the tonic spiking Si3s into bursting state and also controls the delay between burst initiations of contralateral Si2s and Si3s. Finally adding the contralateral slow excitation from Si2s onto Si3s, causes the tail of Si3 burst.

start by restoring the contralateral inhibitory synapses in the network. The burst duration of the network is based on the burst duration of Si2 pair similar to the previous case. The burst length of Sis depends on the conductance strength of the inhibitory synapses between them, but the range of burst length does not include the desired 2-4 second burst length for the control network.

The burst duration is controlled by the contralateral inhibitory synapses from Si3s onto Si2s. These synapses have slower dynamics compared to the inhibitory synapses between Si2s. As the synaptic strength of contralateral inhibition increases, the burst duration gets shorter. The dependence of network dynamics on contralateral inhibition is given in Fig. 4.7. The control network generates the desired burst duration for $g_{ij} = 0.005$.

In the final part of network assembly, we restore the inhibitory connections between Si3s. These inhibitory connections are imperative for robustness of the rhythm. These inhibitory connections are slow and experimental studies showed that they are not strong enough to

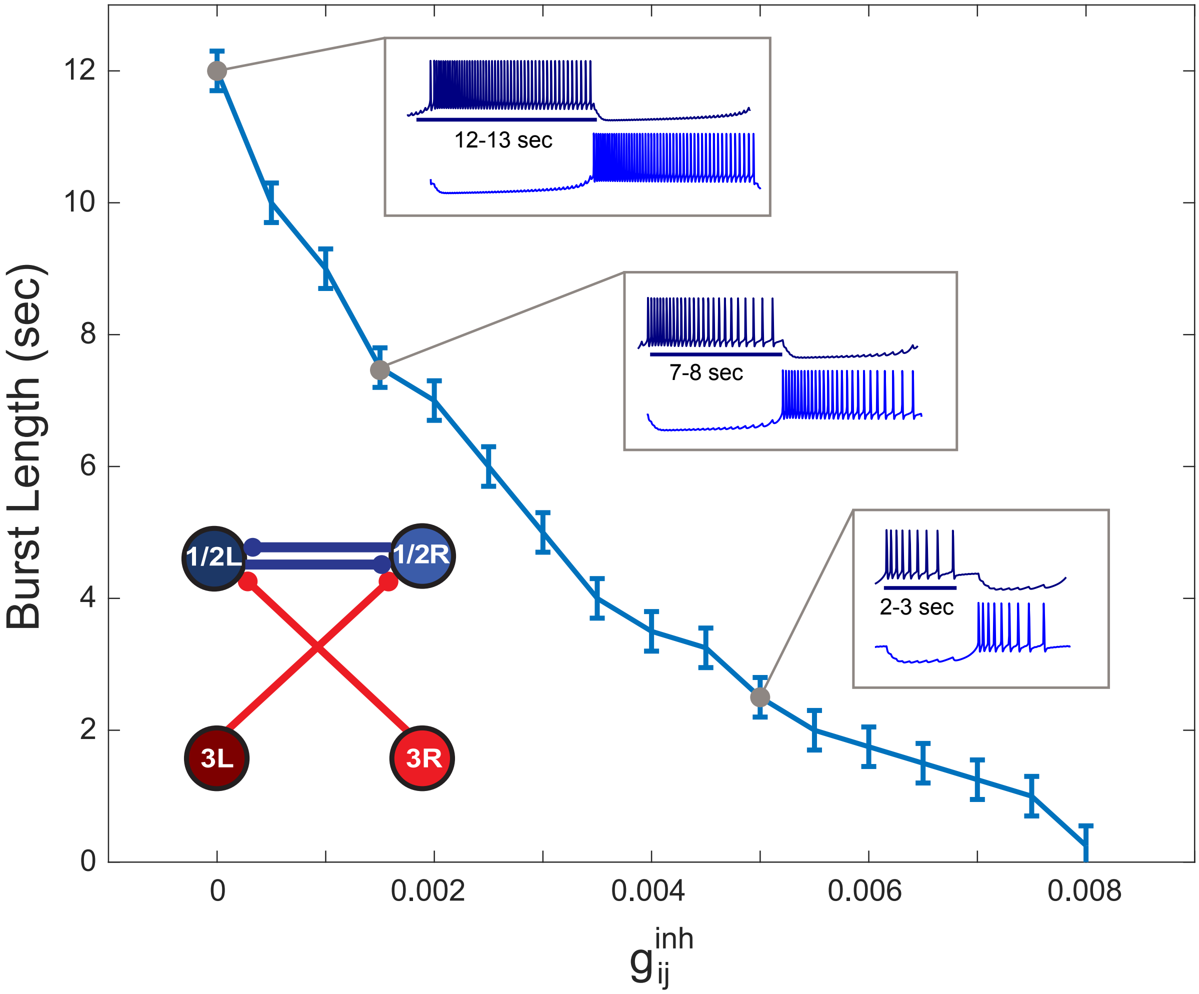

Figure 4.7: Biological CPG generates 2-4 sec long bursts in control case and the model reveals that this burst duration is controlled by inhibition from Si3s onto contraleteral Si2s. The desired burst length of 2-4 sec is produced where $g_{ij} = 0.005$.

initiate the anti-phase bursting activity between Si3s if the Si3 pair is isolated from the whole network. The calibration of the synapses is based on this feature. In summary, they are slow and weaker synapses and have a critical role in generation of the phase locked state between the contralateral Si2s and Si3s.

We have completed the assembly of the network. Now, we need to verify the model by

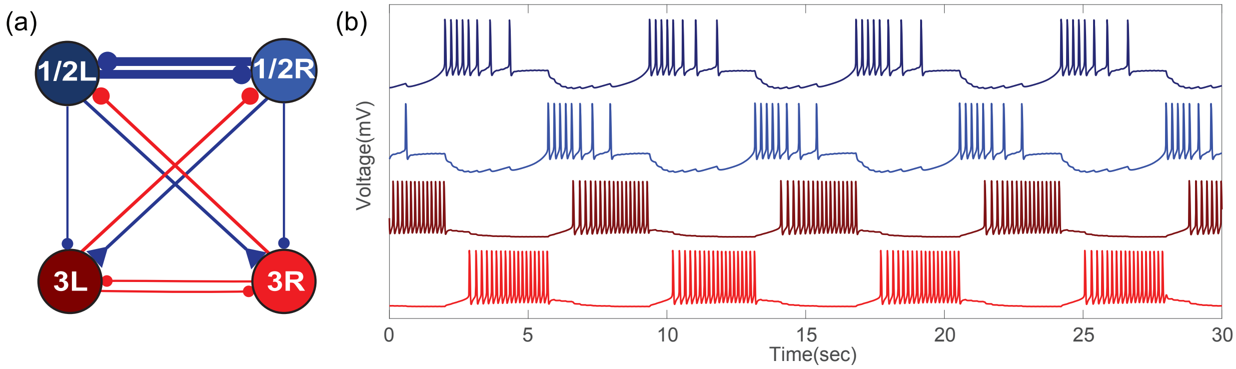

Figure 4.8: Assembling control network for mathematical model. In addition to existing synapses in curare case, the contralateral inhibitory synapses which reduce the burst duration to 2-4 sec like in the experimental studies. Also, the reciprocal inhibition between Si3s plays an important role for the delay between contralateral Si2s and Si3s.

comparing the experimental results and simulation results.

4.4 Model Verification

Our modeling studies are bases on the rhythm generation in two experimental cases: curare and control. We have successfully generated the rhythm in both cases and also showed that the model captures the characteristics of the burst duration and phase locked states in both networks. In this section, we will be comparing the experimental results with the simulation results to verify the model.

For mathematical modeling, we used a reduced network diagram, and we applied a two-step reduction process. The first step of the reduction is ruling out the Si4s. The indirect synapses from Si2s onto Si3s are delayed due to the existence of the Si4s. Instead of generating this delay through Si4s, we used slow synapses from Si2s onto Si3s. (i.e., contalateral excitation and ipsilateral inhibition). The second step of the reduction is merge of Si1s and Si2s. Si1s and Si2s are strongly electrically coupled cells, and due to this strong coupling, their firing pattern is in a highly synchronized manner. Using this feature, we have merged Si1s and Si2s and assumed that ipsilateral cells act as a single cell. When we merged the cells, we merged the inhibitory connections between them as well. In other words, the inhibition between Si2s in the reduced network corresponds to the sum of inhibition between Si1s, inhibition between Si2s and contralateral inhibition between Si1s and Si2s.

Previously, we showed that the burst duration in curare network is controlled by the strength of inhibition between Si2s and dependence of the burst length on coupling strength is given in Fig 3.14. As the synaptic strength gets weaker, the burst duration gets shorter. We would like to verify this characteristic by an experimental result. By voltage clamp method, it is possible to suppress certain cells and record from the rest of the network. In biological curare network, using the voltage clamp technique Si1s are suppressed, and it is observed that during the suppression the burst frequency of the network increases. Which supports our assumption that the synaptic strength of the synapses between Si2s controls the burst duration in curare. By suppressing Si1s, the synapses between Si1s and also the contralateral inhibitory synapses from Si1s onto Si2 are deactivated. Deactivation of these connections can be interpreted in the reduced network as weaker coupling strength between Si2s, so we expect to observe shorter burst duration. This shows that the simulation results meet the experimental results (Fig. 4.9).

The second experimental study we used as verification of the model is the application of an external current to Si1R for a short period during the active phase. Implementation of the external current causes a transition from active phase to quiescent phase of the cell (Si1L)

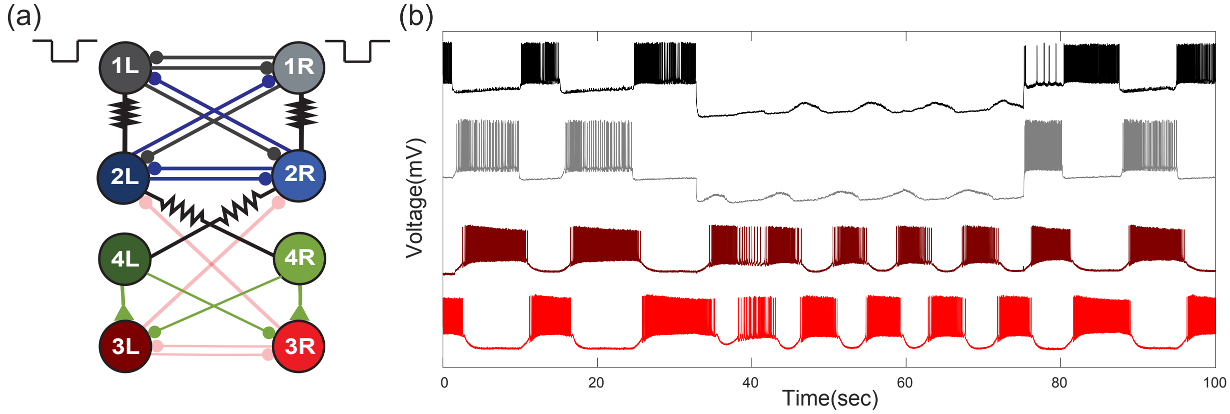

Figure 4.9: (a) The wiring diagram of the full circuit under curare effect where Si1L/R are hyperpolarized through an external current. In other words, it leads to a decrease in the burst duration. The hyperpolarization of the Si1L/R is interpreted as a decrease in the synaptic strength of the inhibitory connections between Si2s in the reduced model.

and as soon as the cell goes to the inactive state, the contralateral pair switches to active phase (Si1R). We implemented the experiment to the mathematical network and applied a hyperpolarizing current to Si2R. It is observed that as soon as Si2R goes to the quiescent phase through the application of external current the contralateral pair becomes active.

The third type of experiments that we used for model verification is hyperpolarizing or depolarizing a single cell in the network via an external current and observe the network dynamics during the application of external current. The first experimental case is hyperpolarizing Si2R during the active swimming. Injecting a hyperpolarizing current to Si2R lead the transition to hyperpolarized quiescent state. Once Si2R goes quiescent, the ipsilateral Si3 switches its state from bursting to tonic spiking state since the hyperpolarization of Si2R deactivates the ipsilateral inhibitory synapse onto Si3R. Unfortunately, we have recordings from only two cells for this experiment, but through the model experiments, it is possible to guess the behavior of the cells in the network. Application of the external current shuts

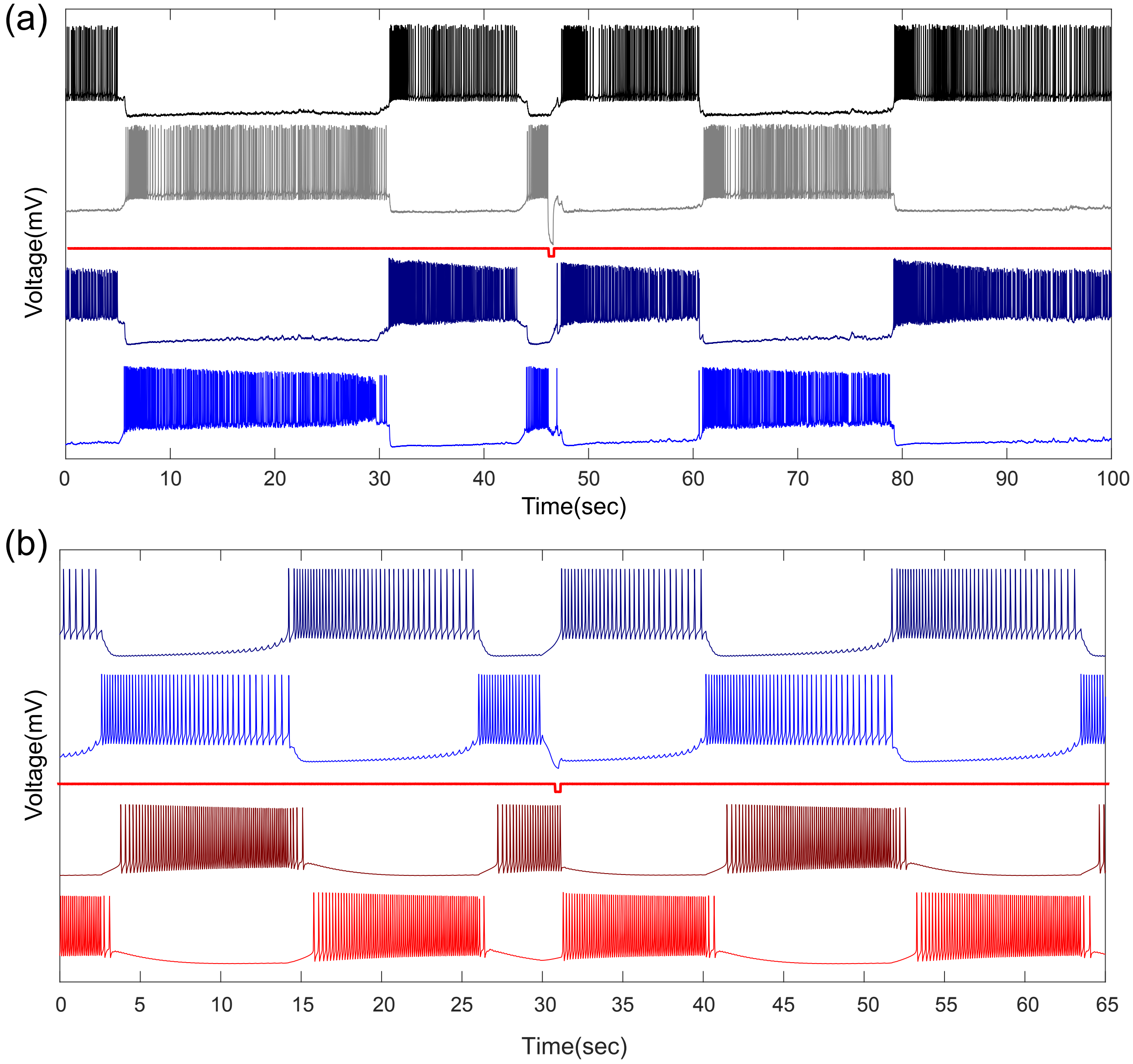

Figure 4.10: Comparing experimental results with simulation results. (a) Recordings from Si1L/R(light/dark gray) and Si2L/R(light/dark blue) with curare in the environment. Application of a hyperpolarizing external current to Si1R during the active phase hyperpolarizes Si1R and activated the contralateral pair (Si1L) immediately. (b) Simulation results for the same experimental design. Applying a hyperpolarizing current to Si2R during the active phase causes the transition of the active cell to quiescent state while activates the contralateral pair immediately.

down Si2R, and this supports Si3R towards tonic spiking state. High-frequency tonic spiking of Si3R promotes strength the inhibitory coupling from Si3R to Si3L and Si3R to Si2L, and these cells go to hyperpolarized quiescent state as well.

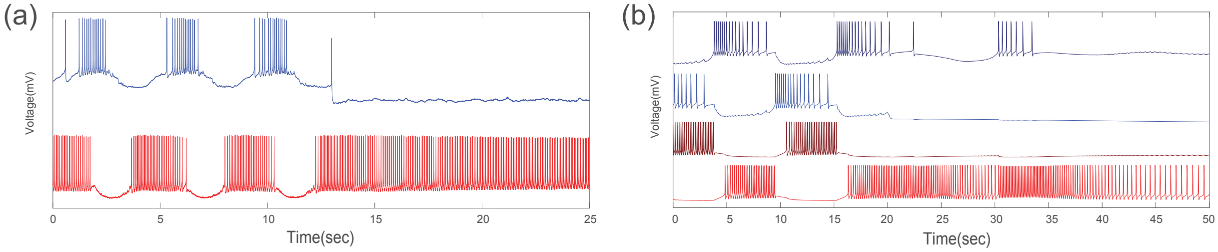

Figure 4.11: Comparing experimental results with simulation results. (a) Recordings from Si2R and Si3R during the swim while Si2R is hyperpolarized. (b) Simulation results from the mathematical network during the swim while Si2R is hyperpolarized.

The second experimental case is opposite of the previous case which is applying a depolarizing external current to Si2R. Through the depolarizing current, the cell becomes a tonic spiking cell. Similar to the previous case, tonic spiking activity promotes the outgoing inhibitory synapses, and throughout this synapses, Si3R and Si2L receive strong inhibition which is strong enough to switch their states to quiescent state. We are able to match the experimental results and modeling results successfully in both cases.

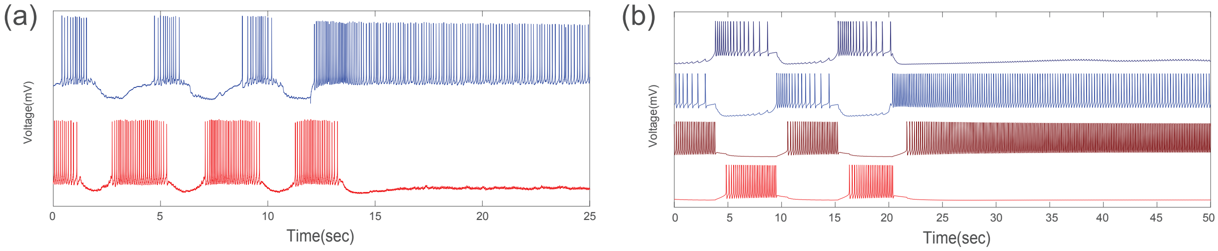

Figure 4.12: Comparing experimental results with simulation results. (a) Recordings from Si2R and Si3R during the swim while Si2R is depolarized. (b) Simulation results from the mathematical network during the swim while Si2R is depolarized.

A similar experiment is designed for Si3s. First, Si3R is hyperpolarized through an external current. Hyperpolarizing Si3R does not stop the network bursting. The network still generates bursting activity, but the characteristics of the bursts slightly change. The network continues generating bursts with prolonged burst duration and smaller interburst interval which means larger duty cycle.

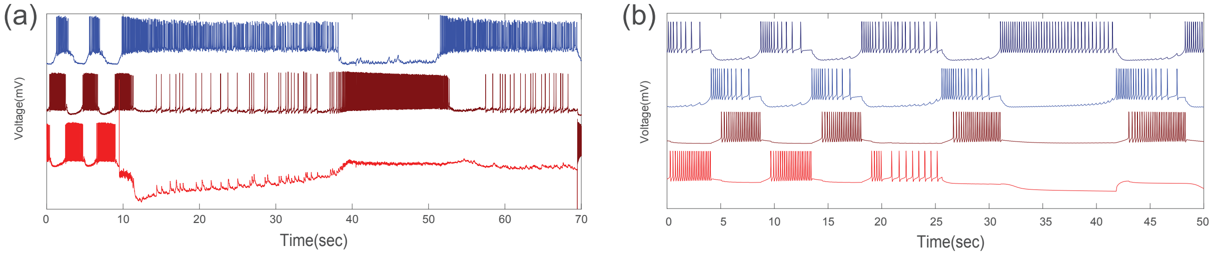

Figure 4.13: Comparing experimental results with simulation results. (a) Recordings from Si2L, Si3L and Si3R during the swim while Si3R is hyperpolarized. (b) Simulation results from the mathematical network during the swim while Si3R is hyperpolarized.

The last experiment is depolarizing Si3R through an external current. Depolarizing current does not stop the network bursting. The network still generates bursting activity, but the characteristics of the bursts slightly change. The network continues generating bursts with prolonged burst duration and smaller inter burst interval which means larger duty cycle.

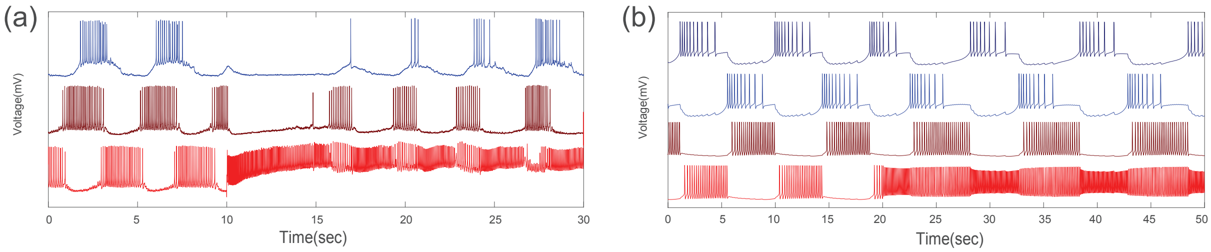

Figure 4.14: Comparing experimental results with simulation results. (a) Recordings from Si2L, Si3L and Si3R during the swim while Si3R is depolarized. (b) Simulation results from the mathematical network during the swim while Si3R is depolarized.

4.5 Summary

In this final stage of our modeling process, we have revised the model according to the recent experimental studies. Earlier we assumed that the Si2 and Si3 pairs follow different mechanisms for HCO generation, but the recent experiments showed that all the cells have similar intrinsic dynamics. TTX is a neuro-toxin which blocks action potential transmission along the axons that connect the contralateral parts of the brain. In other words, disconnects the synapses between two halves of the brain. TTX experiment showed all cells in the mathematical network are tonic spiking cells and Si3s have relatively higher firing frequency compared to Si2s. We set the intrinsic dynamics of the cells according to the experimental results. The firing frequency depends on the Ca bifurcation parameter. As the parameter gets close to the transition border, the firing frequency decreases. The intrinsic dynamics of the cells are set accordingly where Si2s are closer to the boundary. We again followed a similar workflow to assemble the network in the previous chapters successfully assemble the curare and control networks with their characteristics.

As the next step, we have verified our model by implementing the experimental studies to the mathematical model. We have implemented a variety of experimental studies such as dynamic-clamp recordings, external pulses, and application of neuro-blockers. Dynamic-clamp technique is used to recover the inhibitory connections between Si2s while the connections between brain halves are disconnected through TTX. It is observed that as the connection strength increases the burst duration gets longer. This specific characteristic is also verified by application of external currents (see Fig. 4.9). We have verified that the simulation results meet the experimental results of application of depolarizing and hyperpolarizing external currents (Fig. 4.10-4.14).

CHAPTER 5

CONCLUSIONS AND FUTURE DIRECTIONS

Rhythmic behaviors in animals are controlled by small oscillatory neuronal networks called central pattern generators (CPGs) [3]. The focus of this study is to understand the rhythm generation mechanism of Melibe swim CPG. The functional and structural similarities between vertebrate and invertebrate CPGs are a well known phenomena in biology. High complexity level of the vertebrate CPGs and the shared features of them with simple invertebrate CPGs directed researchers towards studies on invertebrate CPGs. The simple structure of invertebrate CPGs is more accessible to analyze and understand the underlying working mechanism. Understanding working mechanism of these simple CPGs provides an insight into the more complex CPGs such as CPGs of mammals, humans. In this aspect, sea slugs are useful and convenient subjects for experimental studies. We are inspired by the extensive empirical studies on the Melibe swim CPG to develop a highly detailed mathematical model for this specific CPG. The Melibe swim CPG network has well identified characteristic features. The focus of earlier modeling studies is generation of the rhythm during the active swimming [27]. Our model development process is classified in three stages. In the first phase, the choice of the model was inspired by firing frequency distribution over a single burst in some of voltage recordings. The bursts have low frequency in the beginning and end, and higher frequency in the middle part of the bursts. This type of bursting behaviour is named as parabolic bursting. The base model was Plant's parabolic bursters model [48, 72] and the synapses were modeled by FTMs [60]. Our goal was to generate active swimming rhythm as in the previous modeling studies. Also, we have reduced the original 8-cell network to a 4-cell network by using the network and synaptic features of the CPG. The first assumption in this part was that all the cells in the reduced network are tonic spiking cells with the same intrinsic dynamics. The Plant's parabolic bursters model originally designed for intrinsic bursters but using bifurcation theory, we were able to set the initial state of the cells to tonic spiking state, and successfully generated the desired rhythm during the active swimming [68] but the model failed to meet other features like the burst duration during the application of neuro-blocker curare. We have also realized that FTM is a good method to model fast synapses but inefficient method for slower synapses.

In the second stage of model development, the experimental results showed that the cells do not burst in isolation. It gave us two options: they are either tonic spiking cells or hyperpolarized quiescent cells. Our first assumption is that the cells do not have the identical individual dynamics and each pair follows different anti-phase bursting mechanism. Again using bifurcation theory, we have terminated the bursting state of the model. According to this assumption, we have set initial dynamics the cells as tonic spiking and quiescent cells. The second assumption was that the synapses have slow dynamics. In this aspect, we have used alpha and dynamic synapse models. Our approach to assembling the network is similar to induction method. We started with intrinsic cell dynamics and continued by the assembly of HCO, curare network and finally the control network which is the network controlling the active swimming behavior. We were able to capture all the features of the network with this setup, but the most recent experimental results showed that the intrinsic dynamics of the cells are quite similar and they are all tonic spikers.

The final stage of the modeling process is assembling the network according to the new experimental findings where all cells are tonic spiking cells. According to the experimental results, Si3s have higher firing frequency than Si2s, and this feature was implemented to mathematical model via bifurcation parameters. Also, in the last stage, we added more details to the model. Each synapse has own characteristic dynamics, so we have defined different coupling functions for each synapse reflecting the specific dynamics of the synapse. Again, we were able to generate the rhythms for curare and control networks with the characteristic features such as burst duration, delay, and tail. Finally, we have verified the model by implementing the biological experiments such as dynamic-clamp recordings and application of external currents to the mathematical network. Comparing the experimental and mathematical results showed the accuracy of the mathematical model.

As mentioned earlier, it is important to understand the underlying mechanisms of this small and simple networks. The insights we gain through this simple networks will provide us the opportunity to develop tools for understanding and analyzing more complex networks in complex animals. Here we explained the development process of a highly detailed mathematical model which captures the almost all characteristics of the Melibe swim CPG. In other words, we have introduced a methodology for development and verification process of a mathematical model. Through this model, it is possible to predict the behavior of the network under different conditions such as external stimulus or deactivation of specific synapses which are not possible to manipulate with neurophysiological methods. Also, the model can also be used to analyze and understand similar CPGs such as Dendronotus swim CPG. There is already an ongoing work about it, and the adjustable dynamics of the model allows it to be used modeling different networks.

REFERENCES

[1] A. Selverston, ed., *Model Neural Networks and Behavior.* Springer, Berlin, 1985.

[2] T. Bal, F. Nagy, and M. Moulins, “The pyloric central pattern generator in crustacea: a set of conditional neural oscillators,” *Journal of Comparative Physiology A*, vol. 163, no. 6, pp. 715–727, 1988.

[3] E. Marder and R. Calabrese, “Principles of rhythmic motor pattern generation,” *Physiological Reviews*, vol. 76, no. 3, pp. 687–717, 1996.

[4] W. Kristan, R. Calabrese, and W. Friesen, “Neuronal control of leech behavior,” *Prog Neurobiol.*, vol. 76, p. 279, 2005.

[5] P. S. Katz and S. Hooper, “Invertebrate central pattern generators,” in *Invertebrate Neurobiology* (G. North and R. R. Greenspan, eds.), New York: Cold Spring Harbor Laboratory Press, NY, 2007.

[6] S. Gillner and P. Wallen, “Central pattern generators for locomotion, with special references to vertebrates,” *Ann. Rev. Neurosci.*, vol. 8, pp. 233–261, 1985.

[7] N. Kopell and B. Ermentrout, “Chemical and electrical synapses perform complementary roles in the synchronization of interneuronal networks,” *Proc. Natl. Acad, Sci.*, vol. 101, no. 43, pp. 15482–15487, 2004.

[8] K. Matsuoka, “Mechanisms of frequency and pattern control in the neural rhythms generators,” *Biol. Cybernetics*, vol. 1, p. 1, 1987.

[9] N. Kopell, “Toward a theory of modelling central pattern generators,” in *Neural Control of Rhythmic Movements in Vertebrates* (A. Cohen, S. Rossingol, and S. Grillner, eds.), New York: Wiley, 1988.

[10] C. C. Canavier, D. A. Baxter, J. W. Clark, and J. H. Byrne, “Multiple modes of activity in a model neuron suggest a novel mechanism for the effects of neuromodulators,” *J Neurophysiol.*, vol. 72, no. 2, pp. 872–882, 1994.

[11] F. Skinner, N. Kopell, and E. Marder, “Mechanisms for oscillation and frequency control in networks of mutually inhibitory relaxation oscillators,” *J Comput Neurosci.*, vol. 1, p. 69, 1994.

[12] R. O. Dror, C. C. Canavier, R. J. Butera, J. W. Clark, and J. H. Byrne, “A mathematical criterion based on phase response curves for stability in a ring of coupled oscillators.,” *Biol Cybern*, vol. 80, no. 1, pp. 11–23, 1999.

[13] A. Prinz, C. Billimoria, and E. Marder, “Alternative to hand-tuning conductance-based models: construction and analysis of databases of model neurons,” *J Neurophysiol.*, vol. 90, no. 6, pp. 3998–4015, 2003.

[14] J. Best, A. Borisyuk, J. Rubin, D. Terman, and W. M., “The dynamic range of bursting in a model respiratory pacemaker network,” *SIAM J. Appl. Dyn. Syst.*, vol. 4, pp. 1107–1139, 2005.

[15] I. Belykh and A. Shilnikov, “When weak inhibition synchronizes strongly desynchronizing networks of bursting neurons,” *Phys Rev Lett*, vol. 101, no. 7, p. 078102, 2008.

[16] W. Sherwood, R. Harris-Warrick, and J. Guckenheimer, “Synaptic patterning of left-right alternation in a computational model of the rodent hindlimb central pattern generator,” *J Comput Neurosci.*, vol. 30, no. 2, p. 323, 2010.

[17] H. Koch, A. J. Garcia, and J.-M. Ramirez, “Network reconfiguration and neuronal plasticity in rhythm-generating networks,” *Integrative and Comparative Biology*, vol. 51, no. 6, pp. 856–868, 2011.

[18] R. L. Calabrese, B. J. Norris, A. Wenning, and T. M. Wright, “Coping with variability in small neuronal networks,” *Integrative and Comparative Biology*, vol. 51, no. 6, pp. 845–855, 2011.

[19] E. Marder, “Neuromodulation of neuronal circuits: back to the future,” *Neuron*, vol. 76, p. 1, 2012.

[20] W. Kristan, “Neuronal decision-making circuits.,” *Curr Biol*, vol. 18, no. 19, pp. R928–R932, 2008.

[21] K. L. Briggman and W. B. Kristan, “Multifunctional pattern-generating circuits.,” *Annu Rev Neurosci*, vol. 31, pp. 271–294, 2008.

[22] J. Wojcik, R. Clewley, J. Schwabedal, and A. Shilnikov, “Key bifurcations of bursting polyrhythms in 3-cell central pattern generators,” *PLoS ONE*, vol. 9, no. 4, 2014.

[23] A. Shilnikov, R. Gordon, and I. Belykh, “Polyrhythmic synchronization in bursting networking motifs,” *Chaos*, vol. 18, no. 3, p. 037120, 2008.

[24] J. Wojcik, R. Clewley, and A. Shilnikov, “Order parameter for bursting polyrhythms in multifunctional central pattern generators,” *Phys Rev E*, vol. 83, pp. 056209–6, 2011.

[25] J. T. C. Schwabedal, A. B. Neiman, and A. L. Shilnikov, “Robust design of polyrhythmic neural circuits,” *Phys. Rev. E*, vol. 90, p. 022715, 2014.

[26] R. E. Change and M. Kim, “Mathematical description of a bursting pacemaker neuron by a modification of the hodgkin-huxley equations,” *Biophys J*, vol. 16, pp. 227–244, 1976.

[27] S. Jalil, D. Allen, J. Youker, and A. Shilnikov, “Toward robust phase-locking in melibe swim central pattern generator models,” *Chaos*, vol. 23, no. 4, p. 046105, 2013.

[28] A. A. Prinz, V. Thirumalai, and E. Marder, “The functional consequences of changes in the strength and duration of synaptic inputs to oscillatory neurons,” *J Neurosci.*, vol. 23, no. 3, pp. 943–954, 2003.

[29] A. A. Prinz, D. Bucher, and E. Marder, “Similar network activity from disparate circuit parameters,” *Nature neuroscience*, vol. 7, no. 12, pp. 1345–1352, 2004.

[30] A. Sakurai, C. A. Gunaratne, and P. S. Katz, “Two interconnected kernels of reciprocally inhibitory interneurons underlie alternating left-right swim motor pattern generation in the mollusk melibe leonina,” *J Neurophysiol.*, vol. 112, no. 6, pp. 317–1328, 2014.

[31] A. Sakurai and P. S. Katz, “The central pattern generator underlying swimming in dendronotus iris: a simple half-center network oscillator with a twist,” *J Neurophysiol.*, vol. 116, no. 4, pp. 1728–1742, 2016.

[32] J. Newcomb, A. Sakurai, J. Lillvis, C. Gunaratne, and P. S. Katz, “Homology and homoplasy of swimming behaviors and neural circuits in the nudipleura (mollusca, gastropoda, opistho-branchia),” *PNAS*, vol. 109, no. 1, pp. 10669–76, 2012.

[33] A. Sakurai, J. Newcomb, J. Lillvis, and P. S. Katz, “Different roles for homologous interneurons in species exhibiting similar rhythmic behaviors,” *Curr. Biol.*, vol. 21, no. 12, pp. 1036–1043, 2011.

[34] A. Sakurai and P. S. Katz, “Distinct neural circuit architectures produce analogous rhythmic behaviors in related species,” *Soc Neurosci Abstr.*, vol. 37.918.04, 2011.

[35] S. Thompson and W. Watson, “Central pattern generator for swimming in melibe,” *J. Exp. Biol.*, vol. 208, no. 7, p. 1347, 2005.

[36] T. Graham-Brown, “The intrinsic factors in the act of progression in the mammal,” *Lond B Biol Society*, vol. 84, no. 572, pp. 308–319, 1911.

[37] L. Ji, J. Zhang, X. Lang, and X. Zhang, “Coupling and noise induced spiking-bursting transition in a parabolic bursting model,” *Chaos: An Interdisciplinary Journal of Nonlinear Science*, vol. 23, no. 1, p. 013141, 2013.

[38] A. Hill, S. Van Hooser, and R. Calabrese, “Half-center oscillators underlying rhythmic movements,” in *The Handbook of Brain Theory and Neural Networks* (M. A. Arbib, ed.), The MIT Press, 2003.

[39] X.-J. Wang and J. Rinzel, “Alternating and synchronous rhythms in reciprocally inhibitory model neurons,” *Ann. Rev. Neurosci.*, vol. 8, pp. 233–261, 1985.

[40] S. Jalil, I. Belykh, and A. Shilnikov, “Fast reciprocal inhibition can synchronize bursting neurons,” *Physi Rev E.*, vol. 81, no. 4, 2, 2010.

[41] S. Jalil, I. Belykh, and A. Shilnikov, “Spikes matter for phase-locked bursting in inhibitory neurons,” *Physi Rev E.*, vol. 85, no. 3, 2, 2012.

[42] D. Perkel and B. Mulloney, “Mechanism of postinhibitory rebound in molluscan neurons,” *Science*, vol. 185, no. 4146, pp. 181–183, 1974.

[43] F. Skinner, N. Kopell, and E. Marder, “Mechanisms for oscillation and frequency control in reciprocally inhibitory model neural networks,” *J Comput. Neurosci.*, vol. 1, no. 1-2, pp. 69–87, 1994.

[44] J. Angstadt, J. Grassmann, K. Theriault, and S. Levasseur, “Mechanisms of postinhibitory rebound and its modulation by serotonin in excitatory swim motor neurons of the medicinal leech,” *J Comp Physiol A.*, vol. 191, no. 8, pp. 715–732, 2005.

[45] N. Kopell and G. Ermentrout, “Mechanisms of phase-locking and frequency control in pairs of coupled neural oscillators,” *Handbook on Dynamical Systems*, vol. 2, pp. 3–54, 2002.

[46] R. Plant and M. Kim, “On the mechanism underlying bursting in the aplysia abdominal ganglion r15 cell,” *Math. Biosci.*, vol. 26, pp. 357–375, 1975.

[47] R. E. Plant and M. Kim, “Mathematical description of a bursting pacemaker neuron by a modification of the hodgkin-huxley equations,” *Biophys J*, vol. 16, pp. 227–244, 1976.

[48] R. Plant, “Bifurcation and resonance in a model for bursting nerve cells,” *J. Math. Biol*, vol. 11, pp. 15–32, 1981.

[49] E. Levitan and I. B. Levitan, “Serotonin acting via cyclic amp enhances both the hyperpolarizing and depolarizing phases of bursting pacemaker activity in the aplysia neuron R15,” *J Neurosci.*, vol. 8, pp. 1152–1161, 1988.

[50] C. Canavier, J. Clark, and J. Byrne, “Simulation of the bursting activity of neuron R15 in aplysia: Role of ionic currents, calcium balance, and modulatory transmitters,” *J Neurophysiology*, vol. 66, no. 6, pp. 2107–2124., 1991.

[51] R. Bertran, “A computational study of the effects of serotonin on a molluscan burster neuron,” *Biol. Cybern.*, vol. 69, pp. 257–267, 1993.

[52] R. Butera, J. W. J. Clark, C. C. Canavier, D. A. Baxter, and J. H. Byrne, “Analysis of the effects of modulatory agents on a modeled bursting neuron: Dynamic interactions

between voltage and calcium dependent systems," *J Comput Neurosci.*, vol. 2, no. 1, pp. 19–44, 1995.

[53] R. Butera, "Multirhythmic bursting," *Chaos*, vol. 8, no. 1, pp. 274–284, 1998.

[54] F. Sieling and R. Butera, "Aplysia R15 neuron," *Scholarpedia*, vol. 6, no. 10, p. 4181, 2011.

[55] A. Shilnikov, "Complete dynamical analysis of a neuron model," *Nonlinear Dynamics*, vol. 68, no. 3, SI, pp. 305–328, 2012.

[56] J. Rinzel and Y. S. Lee, "Dissection of a model for neuronal parabolic bursting," *J Math Biol.*, vol. 25, no. 6, pp. 653–675, 1987.

[57] L. Shilnikov, "Some cases of generation of periodic motion from singular trajectories.," *Math. USSR Sbornik*, vol. 61, no. 103, pp. 443–466, 1963.

[58] V. Afraimovich, S. Gonchenko, L. Lerman, A. Shilnikov, and D. Turaev, "Scientific heritage of L.P. Shilnikov. Part 1.," *Regular and Chaotic Dynamics*, vol. 19, no. 4, pp. 435–460, 2014.

[59] L. Shilnikov, A. Shilnikov, D. Turaev, and L. Chua, *Methods of Qualitative Theory in Nonlinear Dynamics, Parts I and II.* World Scientific Publ., 1998,2001.

[60] N. Kopell and D. Somers, "Rapid synchronization through fast threshold modulation," *Biol. Cybern.*, vol. 68, p. 5, 1993.

[61] S. Daun, J. E. Rubin, and I. A. Rybak, “Control of oscillation periods and phase durations in half-center central pattern generators: a comparative mechanistic analysis,” *J Comput Neurosci.*, vol. 27, no. 1, pp. 3–36, 2009.

[62] A. Destexhe, D. Contreras, T. Sejnowski, and M. Steriade, “A Model of Spindle Rhythmicity in the Isolated Thalamic Reticular Nucleus,” *J Neurophysiol.*, vol. 72, no. 2, pp. 803–818, 1994.

[63] V. Matveev, A. Bose, and F. Nadim, “Capturing the bursting dynamics of a two-cell inhibitory network using a one-dimensional map,” *J Comput Neurosci.*, vol. 23, no. 2, pp. 169–187, 2007.

[64] A. A. Sharp, L. F. Abbott, and E. Marder, “Artificial electrical synapses in oscillatory networks,” *J Neurophysiol.*, vol. 67, no. 6, pp. 1691–1694, 1992.

[65] A. A. Sharp, M. B. O’Neil, L. Abbott, and E. Marder, “The dynamic clamp: artificial conductances in biological neurons,” *Trends in Neurosciences*, vol. 16, no. 10, pp. 389 – 394, 1993.

[66] A. A. Sharp, M. B. O’Neil, L. Abbott, and E. Marder, “Dynamic clamp: computer-generated conductances in real neurons,” *J Neurophysiol.*, vol. 69, no. 3, pp. 992–995, 1993.

[67] H. Van der Loos and E. Glaser, “Autapses in neocortex cerebri: synapses between a pyramidal cell’s axon and its own dendrites,” *Brain Research*, vol. 48, no. 355–360, 1972.

[68] D. Alaçam and A. Shilnikov, “Making a swim central pattern generator out of latent parabolic bursters,” *Int J Bifurcat. Chaos*, vol. 25, no. 7, p. 1540003, 2015.

[69] A. Luthi and D. A. McCormick, “H-current,” *Neuron*, vol. 21, no. 1, pp. 9–12, 1998.

[70] N. Kopell and D. Somers, “Rapid synchronization through fast threshold modulation,” *Biol. Cybern.*, vol. 68, p. 5, 1993.

[71] W. N. Frost and P. S. Katz, “Single neuron control over a complex motor program,” *Proc.Nat.Acad. Sc.*, vol. 93, no. 1, pp. 422–426, 1996.

[72] J. Rinzel and Y. S. Lee, “Dissection of a model for neuronal parabolic bursting.,” *J Math Biol*, vol. 25, no. 6, pp. 653–675, 1987.

A Appendix: Chapter 2

The model in this study is adopted from [48]. The dynamics of the membrane potential, V, is governed by the following equation:

$$C_m\dot{V} = -I_{Na} - I_K - I_{Ca} - I_{KCa} - I_{leak} - I_{syn}, \tag{1}$$

where $C_m = 1\mu F/cm^2$ is the membrane capacitance, I_{Na} is the Na^+ current, I_K is the K^+ current, I_{Ca} is the Ca^{+2} current, I_{KCa} is the Ca^{2+} activated K^+ current, I_{leak} is the leak current, I_{syn} is the synaptic current. The fast inward sodium current is given by

$$I_{Na} = g_{Na}m_\infty^3(V)h(V - V_{Na}), \tag{2}$$

where the reversal potential $V_{Na} = 30mV$ and the maximum Na^+ conductance value $g_{Na} = 4nS$. The instantaneous activation variable is defined as

$$m_\infty(V) = \frac{\alpha_m(V)}{\alpha_m(V) + \beta_m(V)}, \tag{3}$$

where

$$\alpha_m(V) = 0.1\frac{50 - V_s}{\exp((50 - V_s)/10) - 1}, \quad \beta_m(V) = 4\exp((25 - V_s)/18), \tag{4}$$

while the dynamics of inactivation variable h is given by

$$\dot{h} = \frac{h_\infty(V) - h}{\tau_h(V)}, \tag{5}$$

where

$$h_\infty(V) = \frac{\alpha_h(V)}{\alpha_h(V) + \beta_h(V)} \quad \text{and} \quad \tau_h(V) = \frac{12.5}{\alpha_h(V) + \beta_h(V)}, \tag{6}$$

with

$$\alpha_h(V) = 0.07\exp((25 - V_s)/20) \quad \text{and} \quad \beta_h(V) = \frac{1}{\exp((55 - V_s)/10) + 1}, \tag{7}$$

where

$$V_s = \frac{127V + 8265}{105} mV. \tag{8}$$

The fast potassium current is given by the equation

$$I_K = g_K n^4 (V - V_K), \tag{9}$$

where the reversal potential is $V_K = -75mV$ and the maximum K^+ conductance value is $g_K = 0.3nS$.The dynamics of inactivation gating variable is described by

$$\dot{n} = \frac{n_\infty(V) - n}{\tau_n(V)}, \tag{10}$$

where

$$n_\infty(V) = \frac{\alpha_h(V)}{\alpha_h(V) + \beta_h(V)} \quad \text{and} \quad \tau_n(V) = \frac{12.5}{\alpha_h(V) + \beta_h(V)}, \tag{11}$$

with

$$\alpha_n(V) = 0.01\frac{55 - V_s}{\exp((55 - V_s)/10) - 1} \quad \text{and} \quad \beta_n(V) = 0.125\exp((45 - V_s)/80). \tag{12}$$

The TTX-resistant calcium current is given by

$$I_{Ca} = g_{Ca} x (V - V_{Ca}), \tag{13}$$

where the reversal potential is $V_{Ca} = 140mV$ and the maximum Ca^{2+} conductance is $g_{Ca} = 0.03nS$. The dynamics of the slow activation variable is described by

$$\dot{x} = \frac{x_\infty(V) - x}{\tau_x(V)}, \tag{14}$$

where

$$x_\infty(V) = \frac{1}{\exp(-0.3(V+40)) + 1} \quad \text{and} \quad \tau_x(V) = 9400ms. \tag{15}$$

The outward Ca^{2+} activated K^+ current is given by

$$I_{KCa} = g_{KCa}\frac{[Ca]_i}{0.5 + [Ca]_i}(V - V_K), \tag{16}$$

where the reversal potential is $V_{Ca} = 140mV$. The dynamics of intracellular calcium concentration is governed by

$$\dot{Ca} = \rho\left[K_c x(V_{Ca} - V) - [Ca]_i\right], \tag{17}$$

where the reversal potential is $V_{Ca} = 140mV$, and the constant values are $\rho = 0.00015mV^{-1}$ and $K_c = 0.00425mV^{-1}$. The leak current is given by

$$I_{leak} = g_L(V - V_L), \tag{18}$$

where the reversal potential $V_L = -40mV$ and the maximum conductance value $g_L = 0.0003nS$. The synaptic current is defined as

$$I_{syn} = \frac{g_{syn}(V_{post} - E_{rev})}{1 + e^{-k(V_{pre} - \Theta_{syn})}} \tag{19}$$

with the synaptic reversal potential $V_{post} = -80mV$ for inhibitory synapses and $V_{post} = 40mV$ for excitatory synapses and the synaptic threshold $\Theta_{syn} = 0mV$, and $k = 100$.

B Appendix: Chapter 3 & 4

The model in this study is adopted from [48]. The dynamics of the membrane potential, V, is governed by the following equation:

$$C_m\dot{V} = -I_{Na} - I_K - I_{Ca} - I_{KCa} - I_h - I_{leak} - I_{syn}, \tag{20}$$

where $C_m = 1\mu F/cm^2$ is the membrane capacitance, I_{Na} is the Na^+ current, I_K is the K^+ current, I_{Ca} is the Ca^{+2} current, I_{KCa} is the Ca^{2+} activated K^+ current, I_{leak} is the leak current, I_{syn} is the synaptic current. The fast inward sodium current is given by

$$I_{Na} = g_{Na}m_\infty^3(V)h(V - V_{Na}), \tag{21}$$

where the reversal potential $V_{Na} = 30mV$ and the maximum Na^+ conductance value $g_{Na} = 4nS$. The instantaneous activation variable is defined as

$$m_\infty(V) = \frac{\alpha_m(V)}{\alpha_m(V) + \beta_m(V)}, \tag{22}$$

where

$$\alpha_m(V) = 0.1\frac{50 - V_s}{\exp((50 - V_s)/10) - 1}, \quad \beta_m(V) = 4\exp((25 - V_s)/18), \tag{23}$$

while the dynamics of inactivation variable h is given by

$$\dot{h} = \frac{h_\infty(V) - h}{\tau_h(V)}, \tag{24}$$

where

$$h_\infty(V) = \frac{\alpha_h(V)}{\alpha_h(V) + \beta_h(V)} \quad \text{and} \quad \tau_h(V) = \frac{12.5}{\alpha_h(V) + \beta_h(V)}, \tag{25}$$

with

$$\alpha_h(V) = 0.07\exp((25 - V_s)/20) \quad \text{and} \quad \beta_h(V) = \frac{1}{\exp((55 - V_s)/10) + 1}, \tag{26}$$

where

$$V_s = \frac{127V + 8265}{105} mV. \tag{27}$$

The fast potassium current is given by the equation

$$I_K = g_K n^4 (V - V_K), \tag{28}$$

where the reversal potential is $V_K = -75mV$ and the maximum K^+ conductance value is $g_K = 0.3nS$.The dynamics of inactivation gating variable is described by

$$\dot{n} = \frac{n_\infty(V) - n}{\tau_n(V)}, \tag{29}$$

where

$$n_\infty(V) = \frac{\alpha_h(V)}{\alpha_h(V) + \beta_h(V)} \quad \text{and} \quad \tau_n(V) = \frac{12.5}{\alpha_h(V) + \beta_h(V)}, \tag{30}$$

with

$$\alpha_n(V) = 0.01 \frac{55 - V_s}{\exp((55 - V_s)/10) - 1} \quad \text{and} \quad \beta_n(V) = 0.125\exp((45 - V_s)/80). \tag{31}$$

The TTX-resistant calcium current is given by

$$I_{Ca} = g_{Ca} x (V - V_{Ca}), \tag{32}$$

where the reversal potential is $V_{Ca} = 140mV$ and the maximum Ca^{2+} conductance is $g_{Ca} = 0.03nS$. The dynamics of the slow activation variable is described by

$$\dot{x} = \frac{x_\infty(V) - x}{\tau_x(V)}, \tag{33}$$

where

$$x_\infty(V) = \frac{1}{\exp(-0.3(V+40)) + 1} \quad \text{and} \quad \tau_x(V) = 9400ms. \tag{34}$$

The outward Ca^{2+} activated K^+ current is given by

$$I_{KCa} = g_{KCa}\frac{[Ca]_i}{0.5 + [Ca]_i}(V - V_K), \tag{35}$$

where the reversal potential is $V_{Ca} = 140mV$. The dynamics of intracellular calcium concentration is governed by

$$\dot{Ca} = \rho\left[K_c x(V_{Ca} - V) - [Ca]_i\right], \tag{36}$$

where the reversal potential is $V_{Ca} = 140mV$, and the constant values are $\rho = 0.00015mV^{-1}$ and $K_c = 0.00425mV^{-1}$. The h-current is given by

$$I_h = g_h(1/(1 + exp(-(V - 63)/7.8)))^3 y(V - V_h), \tag{37}$$

where the reversal potential is $V_h = 70mV$, and the maximum h-current conductance value is $g_h = 0.0006nS$. The dynamics of the h-current activation variable is described by

$$\dot{y} = 0.5((1/(1 + exp(10(V - 50)) - y)/(7.1 + 10.4/(1 + exp((V + 68)/2.2))), \tag{38}$$

The leak current is given by

$$I_{leak} = g_L(V - V_L), \tag{39}$$

where the reversal potential $V_L = -40mV$ and the maximum conductance value $g_L = 0.0003nS$. The fast threshold modulation (FTM) is defined as

$$I_{FTM} = \frac{g_{syn}(V_{post} - E_{rev})}{1 + e^{-k(V_{pre} - \Theta_{syn})}} \tag{40}$$

with the synaptic reversal potential $V_{post} = -80mV$ for inhibitory synapses and $V_{post} = 40mV$ for excitatory synapses and the synaptic threshold $\Theta_{syn} = 0mV$, and $k = 100$. The alpha synapses are defined as

$$I_{alpha} = g_{syn}S(V_{post} - V_{rev}) \tag{41}$$

alpha synapse dynamics are defined by

$$\dot{S} = \frac{\alpha(1 - S)}{1 + e^{-k(V - V_{th})}} - \beta S, \tag{42}$$

where $\alpha = 0.05$ and $\beta = 0.001$. The dynamic synapses are defined as

$$I_{dyn} = g_{syn}SM(V_{post} - V_{rev}) \tag{43}$$

dynamic synapse dynamics are described by

$$\dot{M} = (1/(1 + e^{-(V+40)}) - M)/tau_M \tag{44}$$

where $tau_M = 4000$.